Simulation of surfactant-mediated tipstreaming in a flow-focusing geometry

Jacek K. Wrobel
Department of Mathematics and Center for Computational Science, Tulane University, 6823 St. Charles Avenue, New Orleans, Louisiana 70118, USA

Michael R. Booty, Michael Siegel, and Qiming Wang
Department of Mathematical Sciences and Center for Applied Mathematics and Statistics, New Jersey Institute of Technology, University Heights, Newark, New Jersey 07102, USA

(Received 12 July 2018; published 26 November 2018)

Simulations are performed of a surfactant-laden drop that is stretched by an imposed uniaxial extension flow at infinity with flow focusing provided by two transverse, coaxial, annular baffles placed symmetrically to either side of the drop. The geometry is axisymmetric, with additional symmetry in the transverse plane that contains the drop center. Under suitable conditions, the drop can enter a mode of drop breakup referred to as tipstreaming, in which a thin elongated filament or thread is emitted from the drop ends and which subsequently breaks up into small droplets via capillary instability. The influence that flow focusing has on the conditions required for tipstreaming and on quantities such as the thread radius are investigated by study of sample simulations and the extent of flow focusing is varied by changing the inner or aperture radius of the annular baffles. The surfactant is soluble and bulk-interface surfactant exchange is in the mixed-kinetic or finite-Biot-number regime. The boundary-integral method is used for the underlying two-phase Stokes flow solver, combined with a finite-difference scheme for evolution of adsorbed surfactant on the interface. The dynamics of dissolved bulk phase surfactant is resolved by a large-bulk-Péclet-number asymptotic approach. Results on the conditions for tipstreaming in the simulations are compared to separate experimental results on conditions for tipstreaming in a microfluidic flow-focusing device.

DOI: 10.1103/PhysRevFluids.3.114003

I. INTRODUCTION

Tipstreaming is a mode of drop breakup in which a thin fluid thread is emitted or drawn from the tip of a drop by an extensional flow and where the thread later breaks into a sequence of small droplets via capillary instability. It was first reported by Taylor in his pioneering experiments on drop deformation and breakup in a four-roller mill [1], where it occurred briefly and apparently by chance. More recently, tipstreaming has been attributed to the presence of chemical surfactants, or surface-active agents, and their influence on flow dynamics, which is to reduce the surface tension at interfaces in a multiphase fluid mixture.

Many different types of surfactant are currently in commercial use as detergents, emulsifiers, or foaming and wetting agents in a range of applications from industrial to domestic contexts. Surfactants also occur in nature as biochemical reaction products and are produced by some microorganisms. In addition to supporting natural processes, naturally occurring surfactants are increasingly being adapted to other applications. Descriptions of the properties and uses of surfactants are given in, for example, Refs. [2–4].

In Ref. [5], Stone reviewed the theoretical and experimental understanding of the various modes of drop breakup, including tipstreaming, in macroscale unconfined flows at the time of writing. At

around the same time experimental studies by de Bruijn [6] and by Janssen *et al.* [7,8] found that for surfactant-induced tipstreaming to occur in isolated millimeter-sized drops the viscosity ratio λ of the interior (dispersed) to exterior (continuous) phase fluids needs to be sufficiently small, $\lambda \lesssim 0.1$, and that both the ambient surfactant concentration and the capillary number or strain rate of the deforming flow need to lie within a certain intermediate range. The small dispersed phase droplets that result from tipstreaming have a size of the order of 10 μm, a high surface surfactant concentration, and consequently a low surface tension. In these studies, the key component of the mechanism for tipstreaming, that it requires a large gradient of the surface tension to develop near the pole or tip of a low-viscosity drop in an extensional flow, was explained.

The behavior of drops and fluid interfaces at the microscale is a central theme of microfluidics, where confinement of flow and the need for repeatability or control are important concerns. Configurations in which microfluidic tipstreaming can occur consist of a channel or capillary supplied with a dispersed phase that terminates inside a continuing parallel outer channel or at intersecting cross channels that are supplied with an immiscible continuous phase. Flow focusing can also be introduced, in which the device geometry is modified to cause locally converging and accelerating flow of both phases. In Ref. [9], Anna gave a comprehensive review of drop and interfacial fluid dynamics in the specific context of microfluidics, with and without surfactants. The review also summarized studies on surfactant-mediated tipstreaming in the presence of flow focusing, which is the main topic for investigation here, and among these studies the experiments described in Refs. [10,11] will be given our particular attention. Typical device dimensions here are of the order of 10–300 μm and tipstreaming thread and droplet diameters as small as 200 nm have been reported [9–12].

In this study the boundary integral method is adapted to simulate the dynamics of a tipstreaming drop in an extensional flow by using a hybrid numerical method to resolve the effects of solubility of surfactant in the large-bulk-Péclet-number limit. The hybrid method was introduced in Ref. [13] in the context of an inviscid bubble in two dimensions and was later extended to viscous drops in more general linear two-dimensional (2D) flows [14] and to a 3D axisymmetric uniaxial extension [15]. Since surfactant molecules are typically large relative to their host solvent molecules they diffuse slowly in the bulk, so the bulk Péclet number Pe is large, typically being of the order of 10^6–10^7 for a drop of radius 0.1 mm in an oil-water mixture. Local stretching and contraction of a deforming fluid interface cause surface and bulk surfactant concentrations to move away from equilibrium, resulting in exchange of surfactant between the interface and bulk across a narrow transition layer of width of $O(\mathrm{Pe}^{-1/2})$ relative to the drop radius. The hybrid method introduces a leading-order matched asymptotic reduction of the dynamics in the transition layer to accurately resolve surfactant concentrations and interfacial surface tension in the $\mathrm{Pe} \to \infty$ limit.

Of the many numerical studies of drop deformation and breakup there are three that evoke the surfactant-induced tipstreaming of experiments. Eggleton *et al.* [16] investigated tipstreaming in an axisymmetric uniaxial extension flow, while Bazhlekov *et al.* [17] reported on 3D simulations of drop deformation and breakup, including tipstreaming, in a simple shear flow. In both of these studies the surfactant is insoluble. In recent work [15], we have used the hybrid method to report on deformation and tipstreaming of a drop in an axisymmetric uniaxial extension including surfactant effects with solubility. All three studies use the boundary integral method for the underlying Stokes flow solver and are set in an unbounded geometry. They find, in qualitative agreement with the experimental observations, that there are limitations on the viscosity ratio, surfactant concentration, and capillary number for tipstreaming to occur. In computations using the finite-element method, Suryo and Basaran [18] observed tipstreaming as a possible mode of flow under specific conditions for equal viscosity fluids but without surfactant, in a bounded coflow geometry, and with no flow focusing.

References [19–29] are examples of numerical studies of drop dynamics with soluble surfactant. These either use a finely adapted or refined mesh to resolve surface-bulk exchange of surfactant, with a deformable or nondeformable interface, or simplify the mechanism of surfactant exchange dynamics, or are restricted to artificially small or at most moderate values of Pe. A recent study

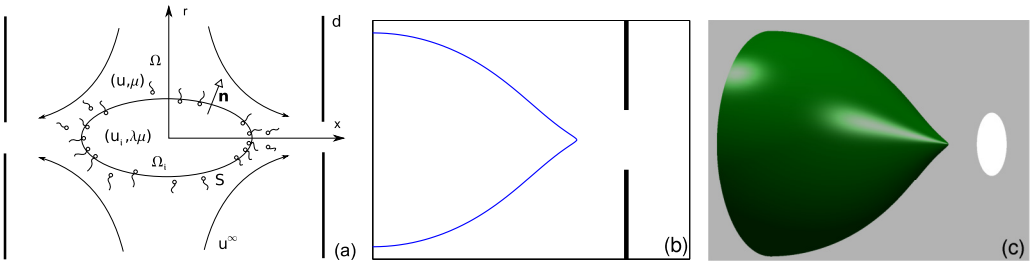

FIG. 1. (a) A drop is situated in a uniaxial extension flow facing a narrow opening in a baffle on either side. The geometry is axisymmetric. (b) Half of the drop in $x > 0$ showing a conical tip, in a 2D profile. (c) The 3D view.

[30] used a fixed uniform mesh with an embedded boundary method to track and resolve interface dynamics with soluble surfactant at nonzero Reynolds number and Péclet number $\mathrm{Pe} = 10^2$.

In this study we consider an isolated, initially spherical drop at the origin of an impulsively started uniaxial extension flow. The interface and continuous phase have a surfactant concentration that is initially in equilibrium, and flow focusing is introduced via transverse annular baffles placed concentric with the flow axis and symmetrically on either side of the drop center. This models the flow focusing of the experimental coflow device [10,11] but does not include its channel sidewalls. Also, we consider an initial-boundary-value problem with additional symmetry about the plane $x = 0$, as opposed to the experiments' near semi-infinite geometry and near steady-state operation.

The model setup is described in more detail in Sec. II. Section III contains the governing equations for Stokes flow with soluble surfactant, together with a description of the large-Pe hybrid method, a note on its conservation of surfactant, and the boundary integral equation for the Stokes flow fluid solver. The numerical implementation is outlined in Sec. IV, which includes a note on a soluble surfactant plume in the downstream wake of a drop as a partial validation of the method and code. Section V is the main section on results. We briefly review the influence of surfactant solubility on tipstreaming in an unbounded flow before studying the influence of flow focusing, via baffles, at a sequence of decreasing aperture sizes and increasing surfactant solubility. We then turn to a comparison of our simulation results with the experimental results of Moyle *et al.* on the conditions needed for tipstreaming [11]. To do so, the simulation data are reformulated to closely approximate the same state-space variables used in presenting the data from the experiments. A summary and conclusions are given in Sec. VI.

II. MODEL GEOMETRY

An initially spherical drop has a uniform concentration of surfactant on its interface that is in equilibrium with a uniform concentration of surfactant in the continuous bulk phase outside it. The drop is situated between two annular baffles that have a large outer radius and an inner or aperture radius that is less than the initial radius of the drop. At time $t = 0$ a uniaxial extension flow $\boldsymbol{u}^\infty$ is imposed with its axis x passing through the drop and aperture centers. The geometry is symmetrical about both the x axis and the plane $x = 0$; the baffle apertures tend to focus the flow as it passes through them. An illustration of the setup is given in Fig. 1(a), while an example computation of a 2D profile and the 3D shape of a deformed half-drop interface in $x > 0$ are shown together with the baffle aperture in Figs. 1(b) and 1(c), respectively. Here the capillary number is sufficiently small that the interface is not drawn through the opening.

This is proposed to capture the main features of flow focusing in the microfluidic tipstreaming device of Anna and Mayer [10] and Moyle *et al.* [11]. Figure 2(a) shows a schematic of the experimental device with an image of a steady rounded interface near the aperture W_{or}. The device geometry is rectilinear but the interface becomes nearly axisymmetric close to the aperture, and

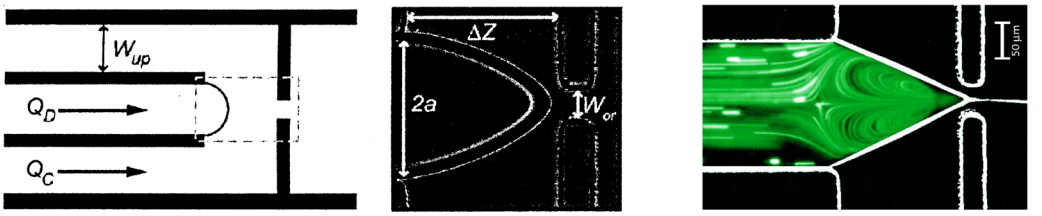

FIG. 2. (a) Schematic diagram (left) indicating flow of the continuous and dispersed phases, and an image (right) of the aperture region with interface not tipstreaming. The dimensions shown are $W_{\rm up} = 280\ \mu$m, $a = 90\ \mu$m, $\Delta Z = 180\ \mu$m, and $W_{\rm or} = 34\ \mu$m. (b) Image showing streaklines in the dispersed phase during formation of a tipstreaming thread (vertical length bar 50 μm). (Figures have been reprinted with permission from Ref. [10].)

surfactant is dissolved in the interior or dispersed phase fluid. Figure 2(b) shows an image of streaklines in the dispersed phase, with a conical interface and a thin tipstreaming thread that is drawn through the aperture. The cited experimental references give a more thorough account of the device and its operation [10,11]. Comparison of the experimental results with our simulation data is given below in Sec. V C.

III. GOVERNING EQUATIONS IN THE LARGE-BULK-PÉCLET-NUMBER LIMIT

The drop has viscosity μ_1, occupies a region Ω_1, and is immersed in an immiscible fluid with viscosity μ_2 that occupies an unbounded exterior region Ω_2. The interface between the two fluids is denoted by S and the surface of a pair of axisymmetric annular rigid baffles is denoted by S_b. In the low-Reynolds-number limit and in the absence of buoyancy or gravitational effects, the flow in each phase is governed by the incompressible Stokes equations

$$\begin{aligned} \lambda\nabla^2\boldsymbol{u} &= \nabla p, \quad \nabla\cdot\boldsymbol{u} = 0, \quad \boldsymbol{x}\in\Omega_1, \\ \nabla^2\boldsymbol{u} &= \nabla p, \quad \nabla\cdot\boldsymbol{u} = 0, \quad \boldsymbol{x}\in\Omega_2, \end{aligned} \tag{1}$$

written in nondimensional form. Here the viscosity ratio $\lambda = \mu_1/\mu_2$. The scale for nondimensionalization of length is the radius a of the unstretched spherical drop. The fluid velocity $\boldsymbol{u}$ is made nondimensional by the capillary velocity $U = \sigma_0/\mu_2$, where σ_0 is the interfacial surface tension in the absence of surfactant. Time is made nondimensional by a/U and the pressure p is made nondimensional by $\mu_2 U/a$.

The fluid velocity is continuous across the interface, which evolves according to the kinematic boundary condition, that is,

$$[\boldsymbol{u}]_1^2 = 0, \quad \boldsymbol{x}\in S, \tag{2}$$

$$\frac{d\boldsymbol{x}}{dt} = (\boldsymbol{u}\cdot\boldsymbol{n})\boldsymbol{n}, \quad \boldsymbol{x}\in S, \tag{3}$$

where $[\cdot]_1^2$ denotes the jump or difference as S is approached from the exterior and interior of S and $\boldsymbol{n}$ is the outward unit normal on S. The stress-balance boundary condition, that the net hydrodynamic traction on S due to the fluid on either side equals the net force acting on S due to interfacial surface tension, is

$$[\boldsymbol{\sigma}]_1^2\cdot\boldsymbol{n} \equiv -(p_2 - p_1)\boldsymbol{n} + 2(\boldsymbol{e}_2 - \lambda\boldsymbol{e}_1)\cdot\boldsymbol{n} = \sigma\kappa\boldsymbol{n} - \nabla_s\sigma, \quad \boldsymbol{x}\in S. \tag{4}$$

Here a subscript denotes the domain, Ω_1 or Ω_2, from which $\boldsymbol{x}$ approaches S, $\boldsymbol{\sigma}$ is the stress tensor, $\boldsymbol{e}_i$ ($i = 1, 2$) is the rate-of-strain tensor, σ is the interfacial surface tension, κ is the sum of the principal

normal curvatures of S, which are chosen to be positive for a convex intersection with S seen from Ω_1, and $\nabla_s = \nabla - \boldsymbol{n}(\boldsymbol{n}\cdot\nabla)$ is the surface gradient operator.

The surface tension σ depends on the concentration of surfactant on the interface Γ according to an equation of state. Here this is taken to be

$$\sigma = 1 + E\ln(1-\Gamma), \tag{5}$$

where the elasticity number $E = RT\Gamma_\infty/\sigma_0$ is a dimensionless measure of the sensitivity of surface tension to variations in surface surfactant concentration, which in turn is made nondimensional by the theoretical maximum monolayer surface concentration Γ_∞. Equation (5) is described as a Langmuir-type surface equation of state [2], the Frumkin surface equation of state [31], or the Szyszkowski surface equation of state [7].

The surface surfactant concentration Γ satisfies the conservation law

$$\left.\frac{\partial\Gamma}{\partial t}\right|_n + \nabla_s\cdot(\Gamma\boldsymbol{u}_s) + \Gamma\kappa u_n = \frac{1}{\mathrm{Pe}_s}\nabla_s^2\Gamma + J\boldsymbol{n}\cdot\nabla C|_S, \quad \boldsymbol{x}\in S. \tag{6}$$

Here the time derivative $\partial_t|_n$ is taken along the direction of the outward normal to the interface when it is in motion and the remaining terms on the left-hand side account for change in Γ due to (i) advection along the interface with the tangential fluid velocity $\boldsymbol{u}_s = \boldsymbol{u} - (\boldsymbol{u}\cdot\boldsymbol{n})\boldsymbol{n}$ and (ii) motion of a locally nonplanar interface along its normal with speed $u_n = \boldsymbol{u}\cdot\boldsymbol{n}$. On the right, the first term describes change in Γ due to surface diffusion, and the surface Péclet number $\mathrm{Pe}_s = aU/D_s$, where D_s is the surface diffusion coefficient. The second term denotes the change in surface surfactant concentration Γ due to exchange with the bulk, where C is the bulk phase surfactant concentration. The rate of exchange is given by the diffusive flux of dissolved surfactant in the bulk phase sublayer immediately adjacent to S and the parameter $J = DC_\infty/\Gamma_\infty U$ is a dimensionless measure of the change in Γ due to this diffusive exchange relative to advection of surfactant on the interface. The bulk surfactant concentration is made nondimensional by an ambient constant far-field value C_∞ and D denotes the diffusion coefficient in the bulk.

The bulk surfactant concentration C advects and diffuses as a passive scalar, so

$$\frac{\partial C}{\partial t} + \boldsymbol{u}\cdot\nabla C = \frac{1}{\mathrm{Pe}}\nabla^2 C, \quad \boldsymbol{x}\in\Omega_2, \tag{7}$$

where the bulk Péclet number $\mathrm{Pe} = aU/D$. Here we take surfactant to be present in the exterior domain alone. The bulk-interface exchange of surfactant satisfies the boundary condition

$$J\boldsymbol{n}\cdot\nabla C|_S = \mathrm{Bi}[K(1-\Gamma)C|_S - \Gamma], \quad \boldsymbol{x}\in S, \tag{8}$$

which equates the diffusive flux of dissolved surfactant in the bulk phase sublayer adjacent to the interface with the local rate of adsorption from the bulk to the interface minus the local rate of desorption from the interface to the bulk. The Biot number $\mathrm{Bi} = a\kappa_d/U$ is the ratio of the flow timescale a/U to the timescale for kinetic desorption κ_d^{-1} and $K = \kappa_a C_\infty/\kappa_d$ is a dimensionless equilibrium partition coefficient with kinetic rate ratio or surface activity κ_a/κ_d.

The initial distribution of bulk surfactant is assumed to be spatially uniform and equal to its constant far-field value, so

$$\begin{aligned} C(\boldsymbol{x},0) &= 1 \quad \text{for } \boldsymbol{x}\in\Omega_2, \\ C &\to 1 \text{ as } |\boldsymbol{x}|\to\infty \quad \text{for all } t>0. \end{aligned} \tag{9}$$

The configuration is in equilibrium initially, so the initial drop shape is spherical, and from (8),

$$\Gamma(\boldsymbol{x},0) = \frac{K}{1+K} \equiv \Gamma_0. \tag{10}$$

The imposed far-field flow that deforms the drop is a uniaxial extension, so

$$\boldsymbol{u}\to\boldsymbol{u}^\infty = \mathrm{Ca}\left(-\frac{r}{2}\boldsymbol{e}_r + x\boldsymbol{e}_x\right) \text{ as } |\boldsymbol{x}|\to\infty, \tag{11}$$

where $\mathrm{Ca} = Ga/U$ is the capillary number and G is the dimensional strain rate of the imposed flow. This is consistent with the flow-focusing geometry since the baffles are finite.

A. Large-bulk-Péclet-number limit

In applications, the bulk Péclet number is large and typically of the order of 10^6–10^7. Since the field equation (7) is singularly perturbed in the limit $\mathrm{Pe} \to \infty$ this led us to introduce a reduced asymptotic model that is derived in this limit in our earlier work [13–15].

The exterior domain Ω_2 is divided into two regions. There is an outer region where spatial gradients in C are not large, which is characterized by a regular approximation of (7). In the $\mathrm{Pe} \to \infty$ limit, the leading-order approximation satisfies

$$(\partial_t + \boldsymbol{u} \cdot \boldsymbol{\nabla})C = 0, \tag{12}$$

so C is constant on particle paths at this order, and with the uniform initial data of (9) this implies that $C \equiv 1$ over much of Ω_2 for $t \geqslant 0$.

When the drop deforms, local change of its interfacial area causes the surface surfactant concentration Γ to depart from its initial equilibrium value Γ_0 of (10). The large bulk Péclet number or slow diffusion of bulk surfactant causes large spatial gradients of C to develop in the normal direction close to the interface, which constitutes a second, inner region or transition layer $\Omega_{2r} \subset \Omega_2$. In this region the dynamics are described by introducing a surface-fitted or intrinsic coordinate system (ξ_1, ξ_2, n) and a stretched normal coordinate $N = n/\epsilon$, in which $C = C(\xi_1, \xi_2, N, t)$. Here n is the distance normal to the interface, with $n > 0$ in Ω_2 and $n = 0$ on S, and ξ_1 and ξ_2 are distance coordinates on S. The system (ξ_1, ξ_2, n) is chosen to be locally orthogonal and the small parameter ϵ is such that $0 < \epsilon = \mathrm{Pe}^{-1/2} \ll 1$.

The bulk surfactant dynamics in the transition layer, written in the intrinsic frame, is governed by

$$(\partial_t + \boldsymbol{v}_s \cdot \boldsymbol{\nabla}_s + \partial_n v_p|_s N \partial_N)C = \partial_N^2 C \quad \text{in } \Omega_{2r}, \tag{13}$$

where

$$\partial_n v_p|_s = -\kappa u_n - \boldsymbol{\nabla}_s \cdot \boldsymbol{u}_s, \tag{14}$$

at leading order [13]. Here $\boldsymbol{v}_s = \boldsymbol{u}_s - \partial_t \boldsymbol{X}|_{\boldsymbol{\xi}}$ is the tangential interfacial fluid velocity relative to a point $\boldsymbol{x} = \boldsymbol{X}(\xi_1, \xi_2, t)$ on the interface with fixed $\boldsymbol{\xi} = (\xi_1, \xi_2)$. The Eulerian fluid velocity $\boldsymbol{u}$, in terms of its projection on the tangent plane $\boldsymbol{u}_t$ and normal component u_p, is $\boldsymbol{u} = \boldsymbol{u}_t + u_p \boldsymbol{n}$, so the normal component of the fluid velocity relative to the interface S is $v_p = u_p - u_n$. This vanishes on S and is approximated by the first term in its Taylor expansion $\partial_n v_p|_s n$ near S. In the intrinsic frame, the time derivative ∂_t of (13) is taken with (ξ_1, ξ_2, N) fixed, and at zero to moderate values of the Reynolds number there is no boundary layer or N dependence of the fluid velocity, so $\boldsymbol{u}_t$ is approximated by the interface tangential fluid velocity $\boldsymbol{u}_s$. As a result, the material derivative and diffusive flux of (7) appear in (13) at leading order, with an error or remainder that is $O(\epsilon)$ as $\epsilon \to 0$. To the same order, Eq. (14) follows from the incompressibility condition (1) when written in the intrinsic frame, and this allows the quantity $\partial_n v_p|_s$ to be found in terms of surface data alone. We note that Wong *et al.* [32] showed that from the first two terms on the left-hand side of Eq. (13) the combination $\partial_t - \partial_t \boldsymbol{X}|_{\boldsymbol{\xi}} \cdot \boldsymbol{\nabla}_s = \partial_t|_n$, which is the time derivative along the outward normal to a moving interface of Eq. (6). Hence (13) can also be written as

$$(\partial_t|_n + \boldsymbol{u}_s \cdot \boldsymbol{\nabla}_s + \partial_n v_p|_s N \partial_N)C = \partial_N^2 C. \tag{15}$$

The initial and boundary conditions become

$$C(\xi_1, \xi_2, N, 0) = 1, \tag{16}$$

with

$$J_0 \partial_N C|_s = \mathrm{Bi}[K(1 - \Gamma)C|_s - \Gamma] \quad \text{on } N = 0 \tag{17}$$

and as

$$N \to \infty \begin{cases} C \to 1 & \text{when } \partial_n v_p|_s \leqslant 0 \\ \partial_N C \to 0 & \text{when } \partial_n v_p|_s > 0. \end{cases} \tag{18}$$

In the bulk-interface surfactant exchange condition (8) we have set $J = \epsilon J_0$, where $J_0 = O(1)$, to form (17). To find the transition layer far-field condition (18) we note that $\partial_n v_p|_s$ is the rate of extension of a fluid line element in the transition layer in the direction normal to S. Where $\partial_n v_p|_s \leqslant 0$, fluid particle paths enter the inner transition layer region from the outer region, which is governed by Eq. (12) with the equilibrium initial value $C = 1$, and so this is the matching value of C as $N \to \infty$. On the other hand, where $\partial_n v_p|_s > 0$, fluid particle paths exit the inner transition layer region. Since bulk-interface surfactant exchange is localized near the interface $N = 0$, C equilibrates far from S to a constant value that is determined by the transition layer dynamics, so the matching condition is $\partial_N C \to 0$ as $N \to \infty$. This constant value of C is then maintained on particle paths in the outer region, per (12), and a wake or plume of dissolved surfactant with $C \neq 1$ develops, leaving the drop interface.

Similar to the formulation of Eq. (17), in the $\mathrm{Pe} \to \infty$ limit, Eq. (6) for evolution of the surface surfactant concentration becomes

$$\left.\frac{\partial \Gamma}{\partial t}\right|_n + \nabla_s \cdot (\Gamma \boldsymbol{u}_s) + \Gamma \kappa u_n = \frac{1}{\mathrm{Pe}_s} \nabla_s^2 \Gamma + J_0 \left.\frac{\partial C}{\partial N}\right|_s \quad \text{on } S. \tag{19}$$

B. Conservation of surfactant

Here we show that the asymptotic model of Sec. III A conserves surfactant in the large-bulk-Péclet-number, small-ϵ limit with an error or remainder of $O(\epsilon^2)$. The integral form of the conservation law (6) for evolution of surfactant Γ on the interface S is

$$\frac{d}{dt} \int_S \Gamma \, dS = J \int_S \frac{\partial C}{\partial n} dS, \tag{20}$$

which includes the influence of surface diffusion and exchange of surfactant with the bulk. For a Lagrangian fluid volume $R \subset \Omega_2$ that is bounded by the drop surface S and a closed surface of material points S_R outside S, Reynolds' transport theorem gives the integral form of the conservation law (7) for bulk surfactant C as

$$\frac{d}{dt} \int_R C \, dV = \frac{1}{\mathrm{Pe}} \int_R \nabla^2 C \, dV. \tag{21}$$

When the divergence theorem is used to express the right-hand side of (21) as the net flux of surfactant entering R across S_R and from S, and the flux integral $\int_S \partial_n C \, dS$ is eliminated via (20), we have

$$\frac{d}{dt} \left(\int_R C \, dV + \frac{1}{J \, \mathrm{Pe}} \int_S \Gamma \, dS \right) = \frac{1}{\mathrm{Pe}} \int_{S_R} \frac{\partial C}{\partial n} dS. \tag{22}$$

Here the normal derivatives are outward on both S and S_R and the relations (20)–(22) are exact.

Each term of Eq. (22) is estimated based on the leading-order asymptotic model of Sec. III A. The surfactant concentrations have expansions in ϵ: $C = C^{(0)} + O(\epsilon)$ and $\Gamma = \Gamma^{(0)} + O(\epsilon)$, and we temporarily restore the (0) superscript on the leading-order terms, which was omitted in Sec. III A.

To estimate $\frac{d}{dt} \int_R C \, dV$, the integral over R is written as the sum of the integral over the inner region of the ϵ-width transition layer Ω_{2r} and over the outer region of its complement $R \setminus \Omega_{2r}$. From Reynolds' transport theorem, each is the integral of the material derivative $\frac{DC}{Dt}$ over the corresponding volume. In Ω_{2r}, the material derivative is given in the intrinsic frame by the left-hand side of Eq. (13) with C replaced by $C^{(0)}$ at leading order, plus a remainder that is $O(\epsilon)$. From Eq. (13) this leading-order term is $\partial_N^2 C^{(0)}$ and the volume element in Ω_{2r} is $dV = \epsilon dN \, dS[1 + O(\epsilon)]$, where terms of the Jacobian that contain the curvature of S are $O(\epsilon)$

throughout. The integration with respect to N across the ϵ-width region Ω_{2r} can be evaluated and the contribution as $N \to \infty$ is zero from the boundary conditions (18). This produces the integral $-\epsilon \int_S \partial_N C^{(0)} dS$ over S plus a remainder that is $O(\epsilon^2)$. To estimate the integral over the outer region $R \setminus \Omega_{2r}$, we note from Eq. (7) that the material derivative is equal to $\epsilon^2 \nabla^2 C$, which is $O(\epsilon^2)$ in the absence of large spatial gradients there. Over R, this gives

$$\frac{d}{dt} \int_R C \, dV = -\epsilon \int_S \frac{\partial C^{(0)}}{\partial N} dS + O(\epsilon^2). \tag{23}$$

The term $\frac{d}{dt} \int_S \Gamma \, dS$ of Eq. (22) is equal to the integral over S of the material derivative $\frac{D\Gamma}{Dt}$ confined to the flow on S, which in turn is given by the left-hand side of (19) with Γ replaced by $\Gamma^{(0)}$ plus a remainder that is $O(\epsilon)$. The leading-order term is given by the right-hand side of (19), with Γ replaced by $\Gamma^{(0)}$ and C replaced by $C^{(0)}$, and the integral of the surface diffusion term is zero since S is closed. Since $J = J_0 \epsilon$ and $1/\mathrm{Pe} = \epsilon^2$, this gives

$$\frac{d}{dt} \left(\frac{1}{J \, \mathrm{Pe}} \int_S \Gamma \, dS \right) = \epsilon \int_S \frac{\partial C^{(0)}}{\partial N} dS + O(\epsilon^2). \tag{24}$$

The left-hand side of Eq. (22) is therefore given by the sum of (23) and (24), in which the $O(\epsilon)$ terms on the right-hand sides cancel to leave an $O(\epsilon^2)$ remainder. The right-hand side of (22) is also of $O(\epsilon^2)$, since the outer boundary S_R of R is in the outer region, where spatial gradients of C are $O(1)$ and $1/\mathrm{Pe} = \epsilon^2$.

We conclude that the hybrid method conserves surfactant at $O(\epsilon)$, with remainder of $O(\epsilon^2)$.

C. Boundary integral formulation

The boundary integral method was chosen to solve the equations for incompressible Stokes flow (1). For a point $\boldsymbol{x}_0$ in the exterior flow domain Ω_2 the fluid velocity $\boldsymbol{u}$ satisfies

$$u_j(\boldsymbol{x}_0) = u_j^\infty(\boldsymbol{x}_0) - \frac{1}{8\pi} \int_S G_{ij}(\boldsymbol{x}, \boldsymbol{x}_0) [\sigma_{ik}(\boldsymbol{x})]_1^2 n_k(\boldsymbol{x}) dS(\boldsymbol{x}) + \frac{1-\lambda}{8\pi} \int_S u_i(\boldsymbol{x}) T_{ijk}(\boldsymbol{x}, \boldsymbol{x}_0) n_k(\boldsymbol{x}) dS(\boldsymbol{x})$$
$$- \frac{1}{8\pi} \int_{S_b} G_{ij}(\boldsymbol{x}, \boldsymbol{x}_0) g_i(\boldsymbol{x}) dS(\boldsymbol{x}), \quad \boldsymbol{x}_0 \in \Omega_2, \tag{25}$$

written in suffix notation. The derivation of (25) in the absence of baffles S_b can be found in Refs. [33,34] and is based on the Lorentz reciprocal identity for Stokes flows and application of the divergence theorem. The free-space Green's function, or Stokeslet, and associated stress tensor, or stresslet, are given by

$$G_{ij}(\boldsymbol{x}, \boldsymbol{x}_0) = \frac{\delta_{ij}}{r} + \frac{\hat{x}_i \hat{x}_j}{r^3}, \quad T_{ijk}(\boldsymbol{x}, \boldsymbol{x}_0) = -6 \frac{\hat{x}_i \hat{x}_j \hat{x}_k}{r^5}, \tag{26}$$

respectively, where $\hat{\boldsymbol{x}} = \boldsymbol{x} - \boldsymbol{x}_0$ and $r = |\hat{\boldsymbol{x}}|$. In the integral over the interface S that contains G_{ij}, or the single-layer potential, $[\sigma_{ik}(\boldsymbol{x})]_1^2 n_k(\boldsymbol{x})$ is the net traction exerted on S by the bulk flow to either side of it, which is given in terms of the interfacial tension by (4). In the integral over S that contains T_{ijk}, or the double-layer potential, u_i is the interfacial fluid velocity on S. The inclusion of rigid baffles S_b introduces two analogous integrals. However, of these, the double-layer term is zero, since the fluid velocity satisfies the no-slip condition $\boldsymbol{u} = 0$ on S_b, and in the single-layer term, which is the last term on the right-hand side of (25), $g_i(\boldsymbol{x})$ is the net traction exerted by the fluid surrounding S_b, which is to be determined.

If $\boldsymbol{x}_0$ approaches S from Ω_2 all terms of (25) are continuous with the exception of the integral for the double-layer potential, which in the limit is given by the sum of a local contribution $4\pi u_j(\boldsymbol{x}_0)$ from a neighborhood of $\boldsymbol{x}_0$ plus the principal value of the integral, which is denoted by $\mathcal{P}V$ and is the value of the improper integral when $\boldsymbol{x}_0$ is on S [34]. After some rearrangement, this gives the integral equation (27a) below. Conversely, if $\boldsymbol{x}_0$ approaches S_b from Ω_2 then all terms of (25) are

continuous, including the double-layer potential, and the fluid velocity $u_j(\boldsymbol{x}_0)$ is zero to satisfy the no-slip boundary condition. After rearrangement, this gives the integral equation (27b). We have

$$u_j(\boldsymbol{x}_0) - \frac{1-\lambda}{4\pi(1+\lambda)} \int_S^{\text{P.V.}} u_i(\boldsymbol{x}) T_{ijk}(\boldsymbol{x}, \boldsymbol{x}_0) n_k(\boldsymbol{x}) dS(\boldsymbol{x}) + \frac{1}{4\pi(1+\lambda)} \int_{S_b} G_{ij}(\boldsymbol{x}, \boldsymbol{x}_0) g_i(\boldsymbol{x}) dS(\boldsymbol{x})$$
$$= \frac{2}{1+\lambda} u_j^{\infty}(\boldsymbol{x}_0) - \frac{1}{4\pi(1+\lambda)} \int_S G_{ij}(\boldsymbol{x}, \boldsymbol{x}_0) [\sigma_{ik}(\boldsymbol{x})]_1^2 n_k(\boldsymbol{x}) dS(\boldsymbol{x}), \quad \boldsymbol{x}_0 \in S, \tag{27a}$$

$$\frac{\lambda-1}{8\pi} \int_S u_i(\boldsymbol{x}) T_{ijk}(\boldsymbol{x}, \boldsymbol{x}_0) n_k(\boldsymbol{x}) dS(\boldsymbol{x}) + \frac{1}{8\pi} \int_{S_b} G_{ij}(\boldsymbol{x}, \boldsymbol{x}_0) g_i(\boldsymbol{x}) dS(\boldsymbol{x})$$
$$= u_j^{\infty}(\boldsymbol{x}_0) - \frac{1}{8\pi} \int_S G_{ij}(\boldsymbol{x}, \boldsymbol{x}_0) [\sigma_{ik}(\boldsymbol{x})]_1^2 n_k(\boldsymbol{x}) dS(\boldsymbol{x}), \quad \boldsymbol{x}_0 \in S_b. \tag{27b}$$

This is a pair of coupled Fredholm integral equations for the fluid velocity $\boldsymbol{u}$ on the drop interface S and the net traction $\boldsymbol{g}$ on the baffles S_b, where the right-hand sides are considered known in terms of the imposed flow $\boldsymbol{u}^{\infty}$ and the net surface traction on S. When $\lambda \neq 1$, Eq. (27a) is of the second kind in $\boldsymbol{u}$ and first kind in $\boldsymbol{g}$, while Eq. (27b) is of the first kind in both $\boldsymbol{u}$ and $\boldsymbol{g}$. When $\lambda = 1$, Eq. (27b) is of the first kind in $\boldsymbol{g}$ while (27a) gives $\boldsymbol{u}$ directly in terms of two single-layer potentials, one over S and one over S_b.

IV. NUMERICAL IMPLEMENTATION

Simplification of (27) occurs since the geometry and flow are axisymmetric about the x axis and symmetric about the plane $x = 0$. In the surface integrals, the integration in the azimuthal direction can be performed analytically, and the components of the Stokeslet and stresslet that result can be expressed in cylindrical (r, x) coordinates in terms of complete elliptic integrals [34,35]. The surface integrals are thus reduced to line integrals over the trace or intersection of the interface S and baffles S_b with a meridional (r, x) plane in the first quadrant $(r > 0, x > 0)$.

Some of the kernels in the line integrals have integrable logarithmic singularities as $\boldsymbol{x} \to \boldsymbol{x}_0$. This occurs in the single-layer potential terms as $\boldsymbol{x} \to \boldsymbol{x}_0 \in S$ on the right-hand side of (27a) and as $\boldsymbol{x} \to \boldsymbol{x}_0 \in S_b$ on the left-hand side of (27b). To resolve these the hybrid Gauss trapezoidal quadrature rules developed by Alpert [36] were used. The quadratures have error of $O(h^p \log h)$, where the choice of the order p determines the nodes and weights, and in this implementation $p = 8$. There are also integrable logarithmic singularities in the kernel of the double-layer potential as $\boldsymbol{x} \to \boldsymbol{x}_0 \in S$ in the principal value integral on the left-hand side of (27a). These were resolved with the boundary element approach of Stone and Leal [37] and eight-point Gauss-Legendre quadrature rules. The discretized system was solved iteratively using the generalized minimal residual method, with tolerance for convergence set to 10^{-13}.

At the beginning of a time step, the surface traction on S is known in terms of the surface tension and the interface shape from (4), so the right-hand side of the system (27) is known; it is then solved iteratively to find $\boldsymbol{u}$ and $\boldsymbol{g}$. The interface position is then updated in time according to the kinematic condition (3), and the updated curvature κ and normal and tangential field $(\boldsymbol{n}, \boldsymbol{t})$ are found on S. With this information, the bulk and surface surfactant concentrations are updated according to Eqs. (13), (14), and (17)–(19), and the equation of state (5) is used to update the surface tension, thereby completing the time step. At predetermined intervals mesh points are redistributed so as to be equally spaced in arc length and more interface mesh points may be added.

The discretization for solving the bulk and surface surfactant concentrations used second-order finite differences in space and the explicit, first-order forward Euler method for the time step. In the absence of baffles, the discretization of Eq. (27a) has the same, second-order, accuracy [15]. However, the overall order of accuracy of the method is lower, and first order in space, when the baffles, which are situated at $x = \pm l$, are introduced. The baffle mesh points on $x = \pm l$ are distributed evenly in the radial coordinate $r \in [r_0, R]$, where r_0 is the aperture radius and the

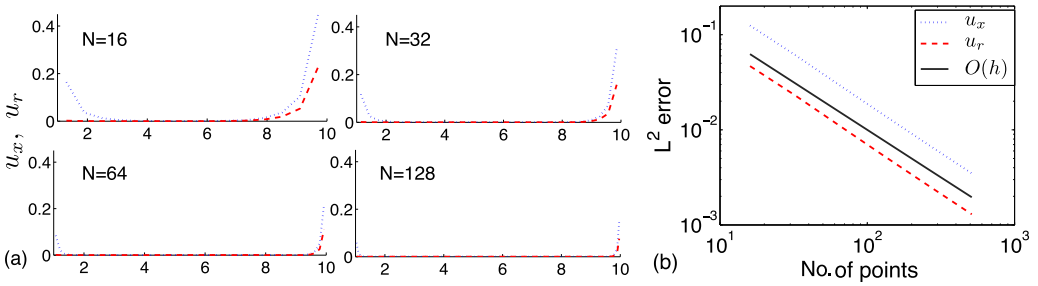

FIG. 3. (a) Velocity components u_x and u_r versus r, evaluated at the midpoint between each of the N computational mesh points on the baffle S_b in the absence of the drop, with values of N from 16 to 128 as indicated in each panel. The baffle occupies the region $r \in [1, 10]$ and $\mathrm{Ca} = 1$. (b) Plot of the L^2 error of the velocity components versus N on log-log scales. The error is of $O(h)$.

outer radius R is fixed at $R = 10$ throughout. The accuracy of implementing the no-slip boundary condition on S_b was verified by evaluating the fluid velocity at midpoints introduced halfway between the baffle mesh points in the absence of the drop. It is given by evaluating the right-hand side minus the left-hand side of (27b) with $\boldsymbol{x}_0$ at each midpoint on S_b. Figure 3(a) shows the axial and radial velocity components u_x and u_r, respectively, evaluated in this way for a typical run with $r_0 = 1.0$ and $\mathrm{Ca} = 1$, when the number of baffle mesh points is doubled sequentially from $N = 16$ to $N = 128$. The error is found to be small everywhere, except near the baffle end points, where it is caused by the singularity of the flow around the sharp aperture edges. The L^2 error of the velocity components on S_b is seen to decrease with $O(h)$, where h is the mesh size, in Fig. 3(b).

Validation and a note on the width of a surfactant plume

In our earlier work [15], the hybrid method and implementation were used to study the dynamics of a drop that is strained by a uniaxial extension with soluble surfactant in the absence of flow focusing baffles. There we noted that it has been validated by comparison with results presented in earlier studies in which the surfactant is insoluble. In particular, it has accurately reproduced the steady-state solutions of Stone and Leal [38] at large and small deformation together with their asymptotic solution in the limit of small capillary number. It has also accurately reproduced the examples of tipstreaming given by Eggleton *et al.* [16].

In Ref. [13] a further partial validation study was performed for steady solutions at small capillary number Ca with soluble surfactant when $E = 0$ and the boundary condition (17) is replaced by $C|_s = 0$. We return to this here. When $E = 0$, the surface tension $\sigma = 1$ and the coupling from the evolution of surface and bulk surfactant to the underlying flow is removed. The fluid velocity and drop shape in the $\mathrm{Ca} \ll 1$ limit have been given in many small-deformation studies (see, for example, [38,39]) and two results that we refer to here are that the drop shape and the rate of extension of a fluid line element normal to the interface $\partial_n v_p|_s$ that appears in Eqs. (13), (14), and (18) are given by

$$\rho = 1 + \mathrm{Ca}\frac{16 + 19\lambda}{8(1+\lambda)}\left(1 - \frac{3}{2}\sin^2\phi\right) + O(\mathrm{Ca}^2), \tag{28a}$$

$$\partial_n v_p|_s = \mathrm{Ca}\frac{3}{1+\lambda}\left(1 - \frac{3}{2}\sin^2\phi\right) + O(\mathrm{Ca}^2), \tag{28b}$$

where ρ and ϕ are the spherical polar distance and the angle of declination from the positive x axis, respectively.

Figure 4 shows the result of a numerical simulation of a drop being strained with capillary number $\mathrm{Ca} = 0.04$ using the hybrid method. This is sufficiently small for the drop shape to be steady with

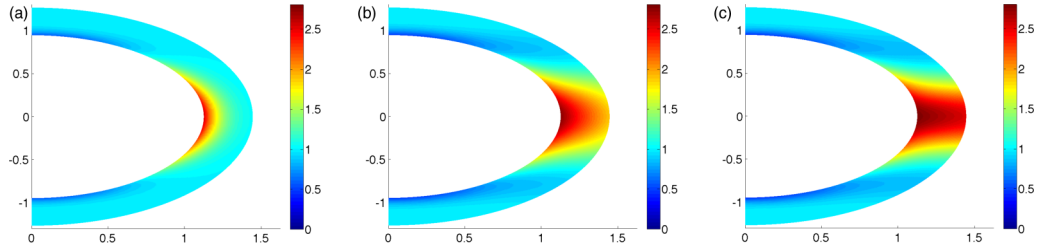

FIG. 4. Drop shape and bulk surfactant concentration with capillary number $\mathrm{Ca} = 0.04$ and initial equilibrium surfactant concentration $\Gamma_0 = 1/3$, shown at times (a) $t = 50$, (b) $t = 200$, and (c) $t = 500$. At the latest time, the surface and transition layer bulk surfactant concentration profiles have reached a steady state. For other parameter values see the text.

small deformation at large times, and the Figs. 4(a)–4(c), which are taken at $t = 50$, 200, and 500, respectively, show the development of a wake or plume of surfactant leaving downstream from the drop. The drop shape appears to be steady throughout this interval, although the data show a small change in the surface concentration of surfactant and surface tension. The other parameter values are $\lambda = 0.05$, $E = 0.2$, $\mathrm{Pe}_s = 10^3$, $J_0 = 0.05$, $K = 0.5$, and $\mathrm{Bi} = 0.1$, some of which will remain fixed throughout the simulations reported later, and the value of the bulk Péclet number, which is introduced only for the presentation of the bulk surfactant concentration data outside the drop, is $\mathrm{Pe} = 10^4$.

The simulation data with surfactant give the drop center to pole distance $\rho(\phi = 0) = 1.111$ and center to equator distance $\rho(\phi = \frac{\pi}{2}) = 0.950$, which are within 3% of the surfactant-free values $\rho(\phi = 0) = 1.081$ and $\rho(\phi = \frac{\pi}{2}) = 0.960$ given by the approximation at Eq. (28a). The slightly more prolate drop shape of the simulation is consistent with the presence of surfactant and decreased surface tension in the simulation data. We define the width of the surfactant plume to be the cylindrical radius at which the flow in the transition layer normal to the interface changes from inflow to outflow, i.e., where $\partial_n v_p|_s = 0$, per Eq. (18). From Eq. (28b) this occurs when $\phi = \sin^{-1}\sqrt{2/3} \simeq 54.7^\circ$, which, neglecting the narrow transition layer width, gives an estimate of the plume width as ~0.816. This is in close agreement with the simulation data at $t = 500$. Near the outer edge of the plume $C < 1$, since it consists of fluid particles that transit the surfactant-depleted part of the transition layer closer to the drop equator, while the plume core is surfactant rich, $C > 1$.

V. RESULTS AND DISCUSSION

In the simulations reported below some dimensionless parameters are held fixed. These include the viscosity ratio $\lambda = 0.05$ and the two parameters associated with insoluble surfactant, $E = 0.2$ and $\mathrm{Pe}_s = 10^3$. It has been noted that it is necessary for $\lambda \lesssim 0.1$ for tipstreaming to occur [5,6] and the value used here is the same as that in the simulations of tipstreaming by Eggleton *et al.* [16]. The chosen value of E is typical of many surfactants and is the same as in other studies [16,17,20,40]. In the asymptotic limit of the hybrid method, the bulk Péclet number Pe is scaled out of the surfactant dynamics as governed by Eqs. (13)–(19), but it must be reintroduced to display spatial data for C, and for this a fixed value of $\mathrm{Pe} = 10^4$ has been chosen. The remaining parameter that is held fixed here is the scaled exchange coefficient J_0 of Eqs. (17) and (19), with $J_0 = 0.05$. Equilibrium initial conditions are assumed throughout, so the initial surface concentration of surfactant and partition coefficient K are related by Eq. (10).

A. Tipstreaming and the influence of Bi in the absence of flow focusing

For reference and comparison with the results to follow, we include a sample of simulations that show the influence of the Biot number Bi on the formation of a filament or thread that tipstreams

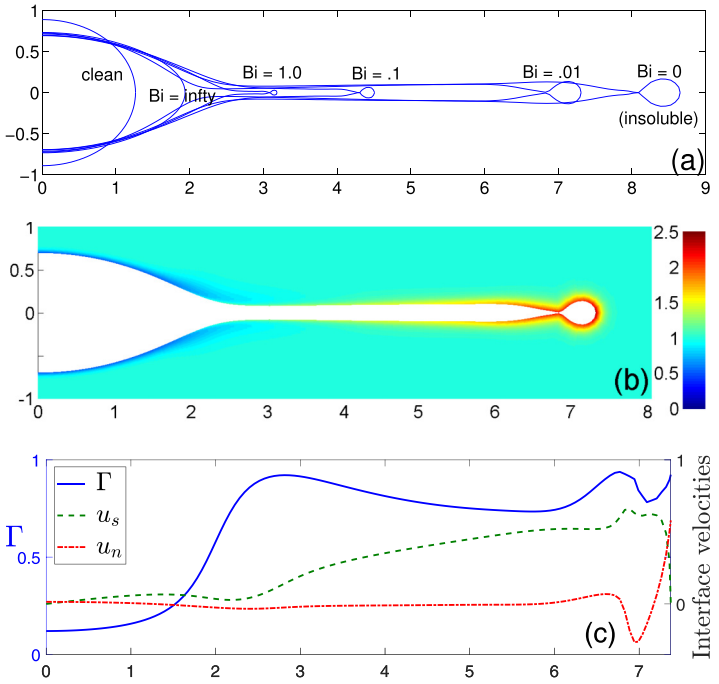

FIG. 5. (a) Surfactant-laden drop, which tipstreams at values of the Biot number indicated when Bi $\lesssim$ 1.0. The main parameter values are $\lambda = 0.05$, Ca $= 0.1$, and the initial surface coverage $\Gamma_0 = 0.6$; for other parameters see the text. Tipstreaming profiles are shown just before pinch-off: in the insoluble limit when Bi $= 0.0$ at time $t = 52.0$ and with surfactant solubility when Bi $= 0.01$ at time $t = 52.0$, when Bi $= 0.1$ at time $t = 64.5$, and when Bi $= 1.0$ at time $t = 88.0$. (b) Bulk surfactant concentration for the simulation of (a) when Bi $= 0.01$. (c) Surface surfactant concentration Γ (left-hand scale) with tangential component u_s and normal component u_n of the interfacial fluid velocity (right-hand scale) versus x.

from a drop in the absence of flow focusing. For this, the capillary number is fixed at Ca $= 0.10$, the equilibrium partition coefficient is fixed at $K = 1.5$, and drop profiles are shown for a range of values of Bi in Fig. 5(a). A tipstreaming thread forms when Bi $\lesssim 1.0$, for which drop profiles are shown at an instant just before the thread is about to pinch off, at a point where a developing tip drop joins the main part of the thread, near its downstream end. We note the trend, which we observed in earlier work at similar parameter values, that as the Biot number increases the thread length just before pinch-off decreases while the radius of the tipstreaming thread and tip drop decrease [15].

When Bi $= 0$ with $J_0 \neq 0$ fixed, the boundary condition (17) implies that the bulk-interface exchange term of Eq. (19) is zero, so in this limit the surface surfactant is insoluble (with $C \equiv 1$ for all $\boldsymbol{x}$ and t). This can also be seen on recalling that Bi $= a\kappa_d/U$ is the ratio of the kinetic rate for desorption to the capillary flow rate, so in the limit when Bi $= 0$ with $K < \infty$ fixed the surfactant exchange kinetics are frozen. With an increase of Bi with J_0 and K fixed the influence of surfactant solubility and bulk-interface exchange steadily increases until, in the limit Bi $\to \infty$, the mixed boundary condition (17) is replaced by the Dirichlet boundary condition

$$C|_s = \frac{\Gamma}{K(1-\Gamma)}. \tag{29}$$

This is referred to as the diffusion-controlled regime [2,31,41]. A large-Péclet-number, bulk surfactant transition layer can still be induced by drop deformation, but the adsorption-desorption exchange kinetics, and the surface and bulk sublayer surfactant concentration $C|_S$, are in local equilibrium at all points on the interface. Figure 5(a) shows a drop profile in this limit that is

completely steady. The profile is also steady for all Bi $\gtrsim 2$, and the figure includes the profile of a steady, clean, or surfactant-free drop ($E = 0$), which at this capillary number is only slightly nonspherical because of its relatively large and uniform surface tension.

Evolution toward the profiles shown in Fig. 5(a) occurs in two phases. Surface surfactant is swept toward the drop pole in the first phase and then a tipstreaming thread forms and evolves in the second phase. When $\mathrm{Pe}_s = \infty$ and either $\mathrm{Bi} = 0$ or $J_0 = 0$, Eq. (6) or (19) for the evolution of Γ implies that surfactant on the interface is frozen into the flow, in the sense that it has the same velocity as a fluid particle at the same point on the interface; in this limit surfactant is sometimes referred to as immobile. Although the simulations are performed with $\mathrm{Pe}_s = 10^3$, this is sufficiently large that the influence of surface diffusion on the data is negligible. In the insoluble limit $\mathrm{Bi} = 0$, or when Bi is small with $J_0 > 0$ and fixed so that the effect of solubility is sufficiently weak, during the first phase surfactant is advected by the flow on the slowly deforming interface toward the drop pole, where it forms a cap of surfactant at high concentration with tangential speed $u_s = |\boldsymbol{u}_s| \simeq 0$, so the interface is nearly immobilized there. There is a substantial surface tension gradient $\partial_s \sigma < 0$ around the outer parts of the cap and very low surface tension in a neighborhood of the cap pole. The second phase begins when viscous stress on the surfactant-immobilized part of the cap near the pole overcomes surface tension to draw the pole out to form the beginning of a tipstreaming thread.

The surface surfactant concentration remains high on the downstream part of the thread. There is axial stretching on the evolving thread interface, both where it is drawn out from the more stationary mother drop and downstream, when it is caused by the x dependence of the axial component of the imposed flow (11). This can occur since the thread is relatively thin, of low viscosity, and because the surfactant is frozen into the flow, or nearly so, so the thread has approximately the same axial speed $u_x = \mathrm{Ca}x$ as the imposed flow. In the early part of the second phase, at times before that of the snapshots in Fig. 5, the transition in radius between thread and mother drop is gradual, with no pronounced shoulder or base to the thread and no discernible tip drop [15]. But by the time that the thread is about to first pinch off due to capillary instability behind the tip drop, which is the time at which the profiles are shown, a thread base is more readily identifiable. The data show that at these times the axial stretching of the thread interface (with rate $\partial_s u_s$) occurs along the thread surface away from the tip drop and is greatest in the region just downstream of the thread base. As a consequence of this stretching, and because of the gradient of Γ on the outer parts of the mother drop surfactant cap from which the thread is drawn, the surface concentration Γ is less along much of the thread than it is further downstream, nearer the tip.

This is borne out by the data of Fig. 5(b) for the bulk surfactant concentration C and Fig. 5(c) for the surface concentration Γ and the tangential and normal components of the interfacial fluid velocity, u_s and u_n, respectively. Here $\mathrm{Bi} = 0.01$ and the effect of solubility on tipstreaming is present but mild. On the downstream part of the thread and tip drop, from $x \simeq 6.0$ to $x \simeq 7.5$, $C|_s > 1.5$ and there is noticeable desorption or leaching of surfactant to the bulk flow, which has had time to develop and spread away from the interface. On the middle part, from $x \simeq 3.2$ to $x \simeq 6.0$, $C|_s \simeq 1.5$, so desorption occurs but is not as evident, and the data of Fig. 5(c) show that u_s is approximately linear in x. From the thread base at $x \simeq 2.5$ up to $x \simeq 3.2$, $1 \lesssim C|_s \lesssim 1.5$ and the desorption is relatively weak. In the vicinity of the thread base $x \simeq 2.5$, C is nonmonotonic in the normal direction; away from the region of weak desorption neighboring the interface, fluid particle paths have exited the surfactant-lean region of the mother drop, where surface surfactant has been depleted by advection and some stretching of the interface, and adsorption from the bulk replenishes it.

As the Biot number is increased, the influence of surfactant solubility is increased and the interface becomes more remobilized. When tipstreaming occurs with increasing Biot number, the thread is significantly shorter in length and is thinner in radius at pinch-off. In the first phase, the surface surfactant concentration remains more uniform while the drop is being deformed, and the high concentration surfactant cap that forms at the pole is smaller. The duration of the first phase is longer at increased Biot number, and the interface shape at the pole has a more pointed tip. When a tipstreaming thread first forms it has a smaller radius, corresponding to the smaller pole cap size.

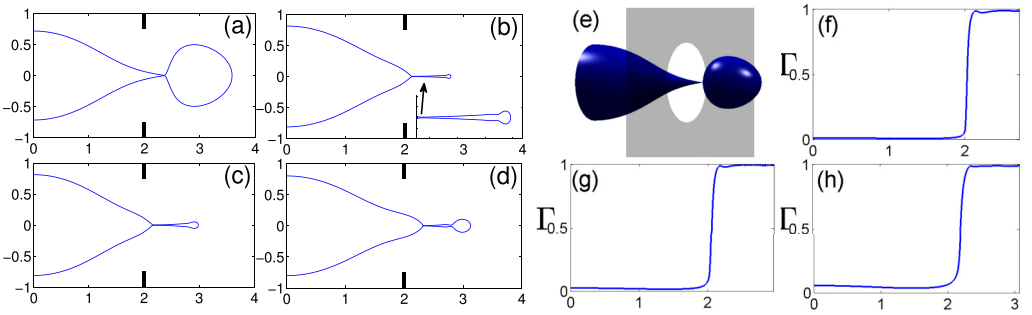

FIG. 6. Insoluble surfactant (Bi = 0) with aperture radius $r_0 = 0.75$ and Ca = 0.74. (a) and (e) Surfactant-free interface ($\Gamma_0 = 0$) shown at time $t = 86.3$, (a) in profile and (e) in perspective. In the remaining panels the interface is surfactant laden, shown in profile just before pinch-off on the left and with the distribution of Γ versus x at the same time on the right, with (b) and (f) $\Gamma_0 = 0.025$ at time $t = 13.2$, (c) and (g) $\Gamma_0 = 0.05$ at time $t = 12.1$, and (d) and (h) $\Gamma_0 = 0.10$ at time $t = 11.5$.

Since the thread remains relatively thin along its length, the duration of the second phase, from tipstreaming to first pinch-off, is relatively short. More discussion on the transition between steady and tipstreaming states is given in Ref. [15], Secs. IV C and IV D.

B. Influence of flow focusing on a tipstreaming thread

Flow focusing is introduced in the form of coaxial axisymmetric annular baffles situated at $x = \pm 2$. This maintains the symmetry of the simulation geometry about $x = 0$ and resembles the flow-focusing geometry of the experiments [10,11]. The baffle outer radius is fixed at $R = 10$, which is large enough for an increase of R to have negligible effect on the flow at the aperture, while the inner radius r_0 takes a sequence of values, at each of which Ca is fixed and Γ_0 and Bi are varied. Other fixed parameters are listed at the beginning of Sec. V. For most of the simulations reported in this section there are $N = 256$ computational mesh points on the interface in the first quadrant ($r > 0, x > 0$) of the (r, x) plane and the time step is $\Delta t = 0.5 \times 10^{-3}$.

1. *Aperture radius* $r_0 = 0.75$

The initial choice of aperture radius is $r_0 = 0.75$, that is, the aperture radius is 0.75 times the initial drop radius. Figure 6 shows a set of simulation data with the capillary number fixed at Ca = 0.74. Surfactant, when present, is insoluble (Bi = 0), and a sequence of relatively low values of the initial surfactant concentration Γ_0 is chosen. In the first, the interface is clean or surfactant-free ($\Gamma_0 = 0$), and the interface is shown in profile in Fig. 6(a) and in perspective in Fig. 6(e) at time $t = 86.3$. The value of Ca = 0.74 is based on this surfactant-free case as being only marginally above the threshold value at which the drop is drawn through the aperture. When Ca is just less than 0.74, the drop shape is steady at large times and has a nearly pointed or conical tip with location $x < 2$. When Ca $\gtrsim 0.74$ the size of the daughter drop when pinch-off is first approached is comparable to the size of the aperture and there is no tipstreaming thread, as seen in Figs. 6(a) and 6(e).

Figures 6(b) and 6(f) show the interface profile and surface surfactant concentration, respectively, at time $t = 13.2$, for an initial uniform equilibrium concentration of insoluble surfactant $\Gamma_0 = 0.025$. In the first phase of the simulation, surfactant is swept to form a cap at the drop pole, which appears to be more or less steady by the time the pole is near the center of the aperture, $x \simeq 2.0$, at time $t \simeq 13.1$. Away from the cap, the interface is almost completely surfactant-free at this time, whereas the concentration is close to the maximum surface concentration over much of the cap. A thin tipstreaming thread is then emitted abruptly, and at the time $t = 13.2$ for which it is shown the thread is about to pinch off at its base, where it joins the mother drop. The maximum radius of the

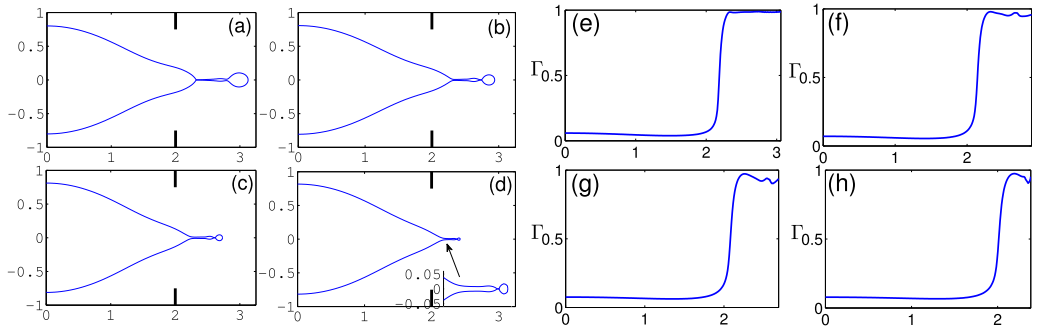

FIG. 7. (a)–(d) Influence of Biot number Bi on drop profiles just before pinch-off and (e)–(h) the corresponding surface surfactant distribution Γ, with $r_0 = 0.75$, Ca $= 0.74$, and $\Gamma_0 = 0.10$. The other parameters are (a) and (e) Bi $= 0$, the insoluble limit, at $t = 11.5$, per Figs. 6(d) and 6(h); (b) and (f) Bi $= 0.10$ at $t = 11.3$; (c) and (g) Bi $= 0.25$ at $t = 11.1$; and (d) and (h) Bi $= 0.50$ at $t = 10.9$.

thread is less than 0.02 and the radius of the thread tip drop is about 0.03. The introduction of flow focusing with a small amount of surfactant has decreased the radius of the thread and tip drop by a factor $\simeq$5 relative to the simulation with insoluble surfactant (Bi $= 0$) in the unconfined geometry of Fig. 5(a), for which $\Gamma_0 = 0.6$, the thread radius is between 0.08 and 0.15, and the tip-drop radius is 0.165. The substantial difference in capillary number Ca between the two simulations (Ca $= 0.10$ vs Ca $= 0.74$) is caused by confinement of the flow that is introduced by the baffles.

At a lower initial concentration $\Gamma_0 < 0.025$, a surfactant cap forms in a way that is similar to that just described and the drop pole forms an almost-pointed, nearly steady, conical tip. However, instead, no tipstreaming thread is formed, and at larger times the drop undergoes a deformation that is qualitatively similar to the surfactant-free case of Figs. 6(a) and 6(e), with the ultimate formation of a large daughter drop downstream of the aperture.

An increase of the initial surfactant concentration from $\Gamma_0 = 0.025$ to $\Gamma_0 = 0.05$ produces dynamics that are qualitatively similar [see Figs. 6(c) and 6(g)], but the accumulating cap of surfactant and the thread and tip-drop radii are larger. For example, in Fig. 6(c), when the thread is first about to pinch off, at its base, $t = 12.1$, and the tip-drop radius is about 0.05. With a further increase to $\Gamma_0 = 0.10$, this trend continues [see Figs. 6(d) and 6(h)], with a near doubling of the tip-drop radius to 0.11. The thread radius is again about to pinch off first at its base, but the tip drop, which is prolate, is now also close to pinch-off.

Solubility of surfactant is introduced to this last example, with $\Gamma_0 = 0.10$ (i.e., $K = 1/9$), by increasing the Biot number Bi from 0 to 0.10, then 0.25, and 0.50. The interface profile and surface surfactant concentration just before pinch-off are shown in Fig. 7, which includes the insoluble (Bi $= 0$) data of Figs. 6(d) and 6(h) for comparison in Figs. 7(a) and 7(e). As the Biot number is increased through this sequence, the thread steadily shortens and becomes thinner. The distance from the thread base to tip-drop end is 0.82, 0.63, 0.48, and 0.23, respectively. There is a similar decrease in size of the tip-drop radius, with sequence 0.11, 0.075, 0.04, and 0.018, respectively. This trend with an increase in Bi is qualitatively similar to that noted without flow focusing in Sec. V A (see Fig. 5) and the data for the fluid velocity on the interface and the surfactant concentrations confirm that it is caused by the same mechanism of surface remobilization with an increase in solubility of surfactant. However, the decrease in radius of the thread with an increase of Bi is much less noticeable when there is flow focusing than it is in unconfined flow; flow focusing has already caused a substantial decrease in thread radius for insoluble surfactant. An additional feature that shows a similar trend in the data sets of Figs. 5(a) and 7 with an increase in Bi is the decrease in prominence of the shoulder between the mother drop and thread base. This is accompanied by a slight decrease in magnitude or spreading out of the surface surfactant gradient $\partial_s \Gamma$ on the part of the shoulder where $0.1 \lesssim \Gamma \lesssim 0.5$.

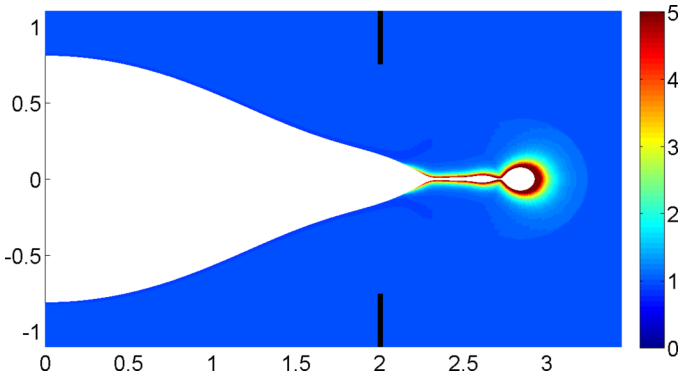

FIG. 8. Bulk surfactant concentration C with the same parameter values and time as in Figs. 7(b) and 7(f).

The effect of solubility on surface surfactant concentration versus axial distance along the thread is seen in Figs. 7(e)–7(h). In Fig. 7(e) surfactant is insoluble (Bi $= 0$) and the surface concentration Γ is nearly uniform and close to the maximum surface concentration along the thread length. As the Biot number and effect of solubility increase through the figure panels, the surface concentration on parts of the thread that were formed at earlier times, i.e., nearer the thread tip, has decreased by up to 10% relative to the value at the thread base, via desorption or leaching from the surface to the bulk flow. A local maximum of the surface concentration is seen at the base of the tip drop, which is close to pinch-off.

Figure 8 shows the bulk surfactant concentration C that corresponds to the profile and surface concentration data for Γ of Figs. 7(b) and 7(f). From the data for the surface concentration of Fig. 7(f), $\Gamma \in (0.94, 0.98)$ on the part of the thread and tip drop for $x \in (2.30, 2.92)$, which is far above the equilibrium concentration of $\Gamma_0 = 0.1$, so surfactant desorbs from the thread surface and enters the bulk in high concentration. This large bulk concentration is clearly visible in Fig. 8. Figure 7(f) also shows that $\Gamma \in (0.050, 0.075)$ on the part of the mother drop for $x \in (0, 1.9)$ and Γ increases to the equilibrium value $\Gamma_0 = 0.1$ at $x \simeq 2.0$. The numerical output confirms that there is mild adsorption from the bulk to the mother drop interface, where $C|_s < 1$, but the effect is too faint to be seen in the color coding of Fig. 8.

We note a difference in the range of surfactant concentration data for the confined flow-focusing simulation of Figs. 7(b), 7(f), and 8 when compared to that for the simulation of unconfined tipstreaming of Figs. 5(b) and 5(c). This causes the apparent loss of resolution in displaying the bulk surfactant data in Fig. 8. In the unconfined example, the surface concentration Γ on the tipstreaming thread is in the range $\Gamma \in (0.7, 0.92)$ relative to an initial equilibrium concentration of $\Gamma_0 = 0.6$, and the bulk concentration C that results is in the range $C \in (0, 2.5)$. In the confined flow-focusing example here, the thread surface concentration [where $\Gamma \in (0.94, 0.98)$] is much further away from the equilibrium concentration ($\Gamma_0 = 0.1$) causing enhanced desorption and larger maximum values of the bulk concentration data, which is now in the range $C \in (0, 5)$, irrespective of the relatively brief duration of the thread. When displaying bulk concentration data the range $C \in (0, 5)$ is maintained throughout the discussion that follows. At this aperture size ($r_0 = 0.75$) the base of the thread, or for the surfactant-free example of Figs. 6(a) and 6(e) the location of the minimum radius, is in the range $x \in (2.10, 2.35)$, which is downstream of the aperture location $x = 2$ in all simulations.

2. Aperture radius $r_0 = 0.50$

The aperture radius is decreased to $r_0 = 0.50$ for a series of simulations at capillary number Ca $= 1.82$. These follow the same path in terms of the initial surface surfactant concentration Γ_0 and the Biot number Bi as in Sec. V B 1. The same criterion is used for choosing the capillary

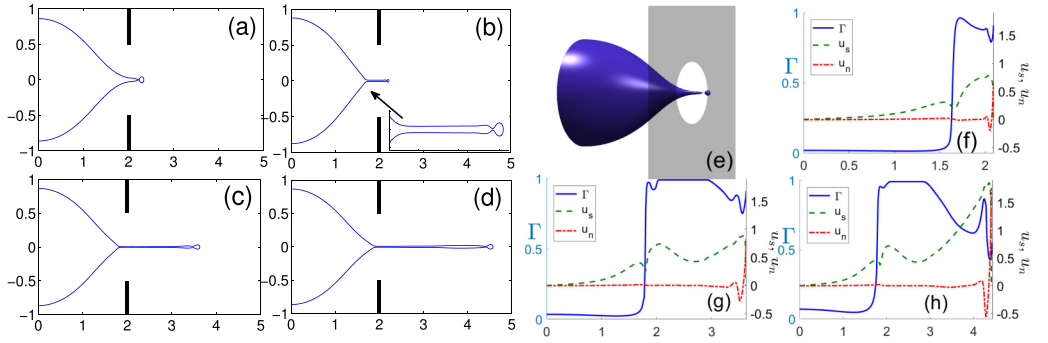

FIG. 9. Insoluble surfactant (Bi = 0) with aperture radius $r_0 = 0.50$ and Ca = 1.82. (a) and (e) Surfactant-free interface ($\Gamma_0 = 0$) shown at time $t = 50$, (a) in profile and (e) in perspective. In the remaining panels the interface is surfactant laden, shown in profile just before pinch-off on the left and with the distribution of Γ and interface velocity components (u_s, u_n) versus x at the same time on the right, with (b) and (f) $\Gamma_0 = 0.025$ at time $t = 7.6$, (c) and (g) $\Gamma_0 = 0.05$ at $t = 9.0$, and (d) and (h) $\Gamma_0 = 0.10$ at $t = 9.5$.

number of the imposed flow: The value Ca = 1.82 in Eq. (11) is just large enough for the drop to be drawn through the aperture when it is surfactant-free. The decrease in aperture size leaves the qualitative trends with change in Γ_0 and Bi mostly unaltered, but it has a more prominent effect on the thread radius and length just before its first pinch-off.

Figure 9 shows the influence of the initial surface surfactant concentration Γ_0 in the absence of solubility effects (Bi = 0) when it is increased through the same sequence $\Gamma_0 = 0.0, 0.025, 0.05, 0.10$ as in Fig. 6. In Figs. 9(a) and 9(e) the interface is surfactant-free ($\Gamma_0 = 0$). In contrast to the surfactant-free case of Figs. 6(a) and 6(e), at this smaller aperture radius the daughter drop pinches off far earlier (at $t = 50$ vs $t = 86.3$) and at a much smaller size. The daughter drop radius is now about 0.04 versus 0.50, which is smaller by an order of magnitude and comparable to the thread and tip-drop sizes seen with surfactant. However, there is no thread formation; instead, a protracted conical tip forms on the mother drop that is similar at both values of r_0 in the surfactant-free case [compare Figs. 6(a) and 9(a)].

Thread formation occurs with the addition of interfacial surfactant. Interface profiles just before pinch-off are shown in Figs. 9(b)–9(d), for which the initial surface coverage Γ_0 is 0.025, 0.05, and 0.10 respectively. The coverage Γ together with the tangential component u_s and normal component u_n of the fluid velocity on the interface just before pinch-off is shown in the corresponding Figs. 9(f)–9(h). The trend of increase in radius of the thread and tip drop with increase in Γ_0 that was observed in Fig. 6 is seen again, but with a sequence of smaller radii so that the effect is less apparent. Here the sequence of tip-drop radii is 0.018, 0.03, and 0.04, with similar values for the maximum thread radius. However, the decrease in aperture radius to $r_0 = 0.50$ causes a noticeable increase in the sequence of thread lengths at pinch-off, which (including tip drop) are now 0.49, 1.82, and 2.69.

The data of Figs. 9(c) and 9(g) show characteristic features that often recur throughout the simulations with $r_0 \lesssim 0.5$. Specifically, in Figs. 9(c) and 9(g), as x increases, insoluble surfactant is advected along the nearly stationary drop interface ($u_n \simeq 0$) while the tangential interface velocity u_s increases due to flow focusing and decreasing drop radius, until u_s reaches a local maximum at the outer edge $x \simeq 1.64$ of the drop's surfactant cap. The interface is then partly immobilized as the drop radius decreases and u_s decreases to a local minimum at $x \simeq 1.80$, at which point the drop surfactant cap merges with the base of the tipstreaming thread and u_s begins to increase. The surfactant concentration Γ continues to increase here due to decreasing drop-thread radius to achieve a local maximum at $x \simeq 1.90$. It is only in the region $1.64 \lesssim x \lesssim 1.90$ of rapid change in Γ that surface diffusion is not negligible. At $x = 1.90$, just upstream of the aperture, the tangential velocity u_s is increasing in x, stretching the thread, and causing Γ to decrease locally. The local minimum

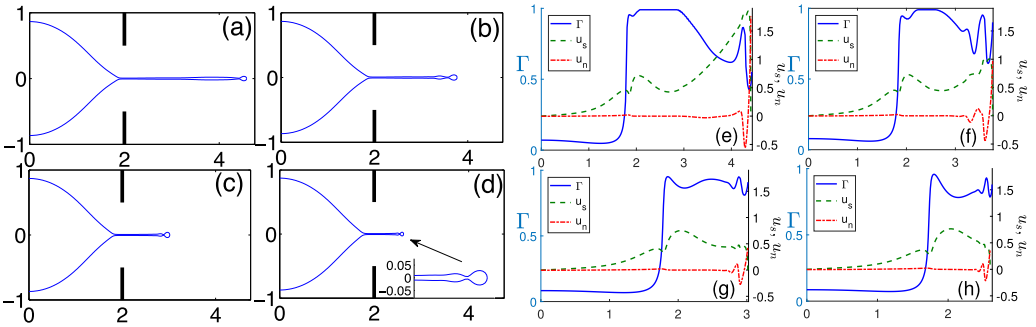

FIG. 10. (a)–(d) Influence of Biot number Bi on drop profiles just before pinch-off and (e)–(h) the corresponding surface surfactant distribution Γ and interface velocity components (u_s, u_n) with $r_0 = 0.50$, $\mathrm{Ca} = 1.82$, and $\Gamma_0 = 0.10$. The other parameters are (a) and (e) $\mathrm{Bi} = 0$, the insoluble limit, at $t = 9.5$, per Figs. 9(d) and 9(h); (b) and (f) $\mathrm{Bi} = 0.10$ at $t = 9.2$; (c) and (g) $\mathrm{Bi} = 0.25$ at $t = 8.4$; and (d) and (h) $\mathrm{Bi} = 0.50$ at $t = 7.8$.

of Γ at $x \simeq 1.97$ and the second local maximum of u_s at $x \simeq 2.04$ are nearly coincident with the aperture location at $x = 2.0$. With an increase of x beyond $x \simeq 2.04$ the flow begins to diverge as it exits the aperture, u_s decreases while Γ remains near the maximum surface concentration, and the local axial compression of the thread is taken up by a slight increase in its radius. Further downstream, away from the baffle, the flow begins to converge again due to the stretching of the imposed flow ($u_x = \mathrm{Ca}x$) and convergence of the flow from around the outer edge of the annular baffle ($R = 10$). As a result, when $x \gtrsim 2.70$ the tangential velocity u_s increases, causing local stretching of the thread and a decrease of Γ away from the maximum surface concentration. This persists until closer to the tip drop, where excursions in u_s, u_n, and Γ are caused by impending pinch-off. Along most of the thread, away from its merger with the mother drop and away from the tip drop, since the surfactant is insoluble and almost diffusion-free, time derivatives are small despite the transient evolution of the thread and $u_n \simeq 0$, the features noted here follow from the observation that the surfactant flux $r_{\mathrm{th}}\Gamma u_s$ is approximately constant, where r_{th} is the thread radius. This is supported by the simulation data.

When compared with the data of Figs. 9(c) and 9(g), in Figs. 9(b) and 9(f) the thread is sufficiently short that it is not influenced by flow divergence on exit from the aperture, while in Figs. 9(d) and 9(h) the thread is sufficiently long that the downstream stretching with increase of u_s that occurs when $x \gtrsim 2.70$ causes a more substantial decrease in Γ, to $\Gamma \simeq 0.63$ just upstream of the tip drop. This last effect, an increase in u_s further downstream from the baffle, is absent in the experiments, since there the flow is confined by parallel channel sidewalls and is driven by controlled fixed-volume flow rates, so that after decelerating on exit from the aperture, u_s remains nearly constant further downstream.

Similar to the introduction of surfactant solubility effects in Sec. V B 1, but with $r_0 = 0.50$ here, next the initial surface concentration is held fixed at $\Gamma_0 = 0.10$ while the Biot number is increased through the same sequence of values: 0.00, 0.10, 0.25, and 0.50. The interface profile and surface surfactant concentration just before pinch-off are shown in Fig. 10, with the data for the insoluble limit ($\mathrm{Bi} = 0$) of Figs. 9(d) and 9(h) shown again for reference in Figs. 10(a) and 10(e). Interface remobilization with increasing Bi causes the thread length from base to tip drop end just before pinch-off to decrease noticeably, in the sequence 2.69, 1.90, 1.15, and 0.87. However, the maximum thread and tip-drop radii are now all in the region from 0.02 to 0.05 and show little or no noticeable trend of decrease with increase in Bi.

At the larger values of $\mathrm{Bi} \gtrsim 0.25$, the thread experiences axial compression as u_s decreases with x due to flow divergence on exit from the aperture, but surfactant solubility and desorption are sufficiently large that the surface concentration Γ stays well below the maximum surface

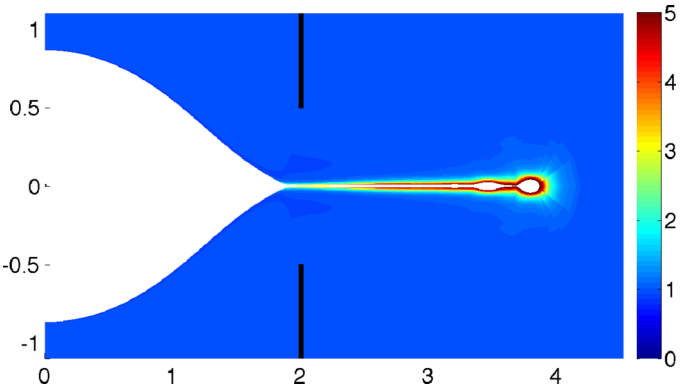

FIG. 11. Bulk surfactant concentration C with the same parameter values and time as in Figs. 10(b) and 10(f).

concentration [see Figs. 10(g) and 10(h)], whereas with $\mathrm{Bi} = 0.10$ this is attained for $2.19 \lesssim x \lesssim 2.66$ [see Fig. 10(f)].

Figure 11 shows the bulk surfactant concentration with the same parameter values and at the same instant as in Figs. 10 (b) and 10(f). Desorption of surfactant from the interface to the bulk flow occurs along the tipstreaming thread and is most noticeable in the vicinity of the tip drop. At the time of the figure, the lifetime of the thread tip since leaving the mother drop is approximately equal to the flow time divided by the capillary number $a/\mathrm{Ca}U$, so the ratio of the tip-drop age to desorption time is of the order of $\mathrm{Bi}/\mathrm{Ca} \simeq 0.05$.

With a decrease in aperture radius from $r_0 = 0.75$ to $r_0 = 0.50$ the location of the thread base has moved from the downstream side to the upstream side of the aperture, in the vicinity $1.7 \lesssim x \lesssim 1.9$.

To explore the evolution of the tipstreaming thread at times beyond its first pinch-off, simulations were continued by closing off the thread interface at its point of minimum radius when this reached a threshold of $\simeq 10^{-3}$ and omitting the excised downstream region of the dispersed phase from the computation at later times. This was repeated at consecutive pinch-off events. In these simulations, the minimum radius usually occurred immediately behind the tip drop, but it also occurred less frequently further upstream along the thread. It is assumed that the omitted interface and dispersed phase droplets have negligible influence on the tipstreaming thread.

Figure 12 shows two examples of this. In both examples, $r_0 = 0.50$, $\mathrm{Ca} = 1.82$, the initial surface surfactant coverage $\Gamma_0 = 0.10$, and these are held fixed. For the data of Fig. 12(a) the Biot number

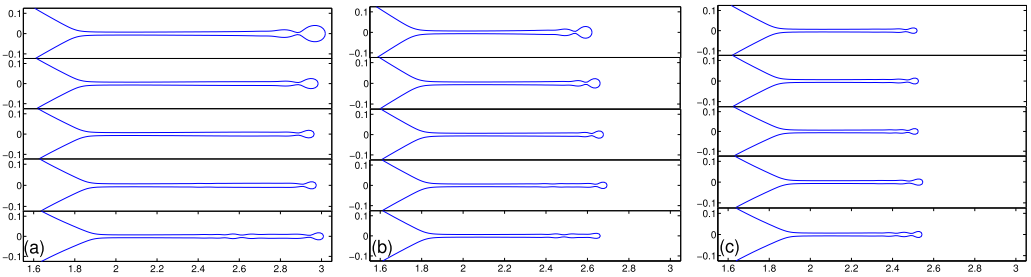

FIG. 12. Thread evolution with aperture radius $r_0 = 0.50$, $\mathrm{Ca} = 1.82$, and $\Gamma_0 = 0.10$. Between each frame a tip drop pinches off; it is then removed from the computation and is not shown in the figure. (a) $\mathrm{Bi} = 0.25$ and the time interval between frames is $\Delta t = 0.3$ with the first (top) frame at $t = 8.4$. (b) $\mathrm{Bi} = 0.50$ and the frame time interval is $\Delta t = 0.3$ with the first (top) frame at $t = 7.8$. (c) $\mathrm{Bi} = 0.50$ and the frame time interval is $\Delta t = 0.2$ with the first (top) frame at $t = 9.2$.

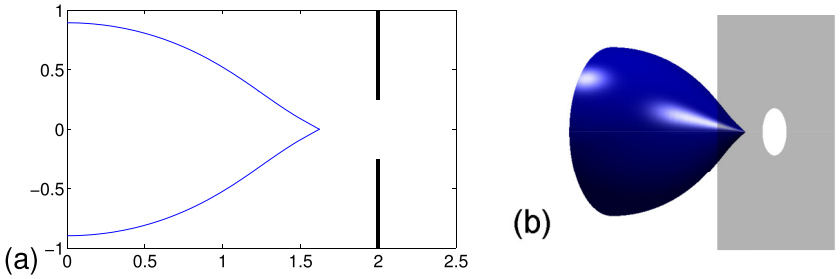

FIG. 13. Steady drop with a conical tip in the absence of surfactant, with the aperture radius $r_0 = 0.25$ and capillary number $\mathrm{Ca} = 12.90$ shown at time $t = 38.6$, in (a) profile view and (b) perspective view.

is set at $\mathrm{Bi} = 0.25$ and the time of the uppermost frame is $t = 8.4$, so this image is a close-up of the tipstreaming thread of Figs. 10(c) and 10(g). The sequence of frames below it are each taken at a fixed time interval of $\Delta t = 0.3$ thereafter, and one tip drop has pinched off and been excised between each consecutive frame. During the time interval spanned by the figure, the evolution appears to be approaching a more or less periodic state with period close to 0.3 in the top four frames, but in the last frame of the panel the thread is less uniform in radius with an apparent neck or capillary instability developing in the region $2.5 \lesssim x \lesssim 2.6$. It is possible that this is a numerical artifact, but refining the computational mesh by doubling the number of node points on the interface suggests this is not so. The precise location and time at which the instability sets in are mildly sensitive to the mesh size and time step but its occurrence appears to be robust.

For the data of Figs. 12(b) and 12(c) the Biot number is increased to $\mathrm{Bi} = 0.50$, and in Fig. 12(b) the time of the earliest (uppermost) frame is $t = 7.8$, so this image is a close-up of the tipstreaming thread of Figs. 10(d) and 10(h). The sequence of frames below it are taken at a fixed time interval of $\Delta t = 0.3$, with a single tip drop having pinched off and been excised between consecutive frames. The thread shows a slight constriction beginning to develop in the fourth frame of Fig. 12(b) at $x \simeq 2.43$. This has moved downstream to $x \simeq 2.48$ in the last frame of Fig. 12(b), in which it is the location of the minimum thread radius, while the thread end is at $x \simeq 2.66$. Between this frame and the time $t = 9.2$ of the earliest (uppermost) frame of Fig. 12(c) the thread has pinched off at $x \simeq 2.50$ and the substantial segment of the end of the thread downstream of this point has been excised; it has two to three times the volume of the single tip drops that were emitted earlier in the simulation. The fixed time interval between subsequent frames in Fig. 12(c) is reduced to $\Delta t = 0.2$ and the sequence of events repeats in a qualitatively similar way at this reduced time interval. Initially, a sequence of single tip drops pinches off between consecutive frames, until a capillary instability begins to form some distance upstream of the thread end at a time around that of the fourth and fifth frames. A resolution study suggests that the main features, the pinching off of either a single tip drop or less frequently a larger section of the thread end, are robust.

3. Aperture radius $r_0 = 0.25$

The aperture radius is decreased further to $r_0 = 0.25$. At this level of flow focusing there is a difference in the behavior of the interface with respect to the capillary number when it is surfactant-free. For values of the capillary number Ca up to 85, which is the largest considered, the drop interface is not drawn through the aperture. Instead, there is a smaller threshold value of the capillary number $\mathrm{Ca}_c \simeq 12.85$, below which the interface approaches a steady state with a rounded shape and tip and above which the interface approaches a steady shape where the pole is drawn into a cone that has a very sharp tip situated closer to the aperture. An example of this is shown in Fig. 13, where $\mathrm{Ca} = 12.90 > \mathrm{Ca}_c$. The transition between the two configurations with increase in Ca appears to be discontinuous.

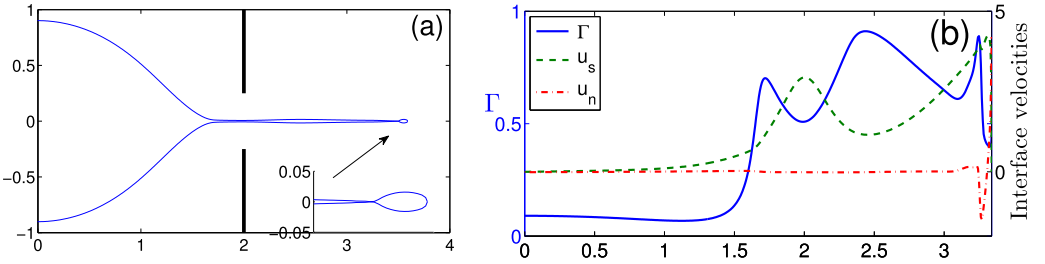

FIG. 14. The addition of insoluble surfactant at initial concentration $\Gamma_0 = 0.10$ but with all other parameters as in Fig. 13 induces tipstreaming. Data are shown just before pinch-off, at time $t = 9.0$. (a) Interface profile. (b) Surface surfactant concentration Γ with tangential component u_s and normal component u_n of the interfacial fluid velocity versus x.

With the capillary number fixed at $\mathrm{Ca} = 12.90$, the presence of insoluble surfactant ($\mathrm{Bi} = 0$) at a relatively modest concentration of $\Gamma_0 = 0.10$ is sufficient to induce tipstreaming. This is seen in Fig. 14(a), which shows the interface, thread, and tip drop just before pinch-off at $t = 9.0$. The tip drop and maximum thread radius are both $\simeq$0.016, the thread length is $\simeq$1.90, and pinch-off is about to occur at the juncture between thread and tip drop. At smaller initial concentrations $\Gamma_0 \lesssim 0.1$ thread formation was not observed.

When surfactant solubility is introduced with $\mathrm{Bi} = 0.10$ but with all other parameters unchanged the thread is considerably shorter and narrower at the instant just before pinch-off. This is seen in Fig. 15, for which the time $t = 7.6$. Figure 15(a) shows the interface profile at this time, with tip-drop radius $\simeq$0.011 and thread radius just behind the pinch-point nearly constant at $\simeq$0.007 over a length $\Delta x \simeq 0.3$. The tendency of solubility to result in a thread that is noticeably shorter and slightly narrower was noted above at larger aperture radii.

The shoulder or decrease in radius where the mother drop merges with the thread is more gradual here, both with and without surfactant solubility, than was found at the larger aperture radii discussed above, to the extent that the location of a thread base is not as clearly identifiable in the interface profiles. The decrease in aperture radius from $r_0 = 0.75$ has caused the region of drop-thread merger to move continually upstream, until it is located in the region $1.50 \lesssim x \lesssim 1.65$ when $r_0 = 0.25$, and the more gradual decrease in interface radius corresponds to the slower rate of convergence of the flow further upstream away from the aperture.

However, the data of Figs. 14(b) and 15(b) show a point where a fairly sharp increase in the interfacial stretch rate $\partial_s u_s$ occurs. This is at $x \simeq 1.63$ with insoluble surfactant in Fig. 14(b) and is more visible at $x \simeq 1.52$ with soluble surfactant in Fig. 15(b). We take this to be the point of demarcation between the mother drop and tipstreaming thread. Returning to Fig. 14(b), although the interfacial stretch rate is positive and increasing with x near the drop-thread merger at $x \simeq 1.63$, there is a decrease in interface radius there that is sufficient to cause a fairly rapid increase in the

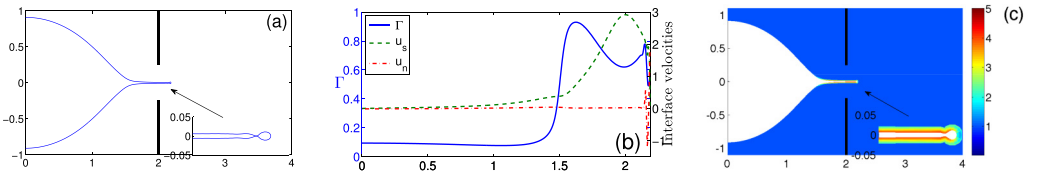

FIG. 15. The inclusion of surfactant solubility with $\mathrm{Bi} = 0.1$ but with all other conditions as in Fig. 14 leads to a shorter and slightly narrower thread just before pinch-off, at time $t = 7.6$, with aperture size $r_0 = 0.25$, capillary number $\mathrm{Ca} = 12.90$, and $\Gamma_0 = 0.10$. (a) Interface profile. (b) Surface surfactant concentration Γ and interfacial fluid velocity components (u_s, u_n) versus x. (c) Bulk surfactant concentration C.

TABLE I. Data for the geometry, fluid, and surfactant properties in the experiments reported by Moyle *et al.* [11], with other data as indicated. (Data have been reproduced with permission from Refs. [10,11].)

Property description	Symbol	Value
width of continuous phase feed channels	$w_c \equiv W_{\text{up}}$	285 μm
half-width of dispersed phase channel	a	94 μm
length from channel merger to focusing aperture	$L \equiv \Delta Z$	190 μm
width of focusing aperture	w_{or}	38 μm
viscosity of continuous phase	μ_2	40 cP
viscosity of dispersed phase	μ_1	1 cP
oil-water clean interface surface tension	σ_0	62 mN/m
interfacial surfactant maximum packing concentration	Γ_∞	2.25 μmol/m^2
kinetic desorption rate constant	κ_d	6.86×10^{-6} s^{-1}
kinetic adsorption rate constant	κ_a	22.1 m^3/(s mol)
bulk surfactant diffusivity[a]	D	10^{-10} m^2 s^{-1}
bulk surfactant concentration range[b]	C_∞	$1.5 \times 10^{-2} \leqslant C_\infty \leqslant 1.5$ mol/m^3
capillary velocity scale	U	$U = \sigma_0/\mu_2 = 1.55$ m s^{-1}

[a]This representative value is given in various studies [31,41–44].

[b]The value at critical micelle concentration (CMC) given by Anna and Mayer [10] is $C_\infty = 10^{-1}$ mol/m^3.

surface surfactant concentration Γ, until it attains a local maximum of $\Gamma \simeq 0.70$ at $x \simeq 1.69$. The thread then experiences increased stretching followed by compression during its transit across a neighborhood of the aperture at $x = 2.0$. The local maximum of u_s and local minimum of Γ at $x \simeq 2.0$ are clearly visible in the figure, and the thread radius of 0.005 there is close to the limit that the computations can resolve before indicating pinch-off. Downstream of the aperture, the region of flow divergence and interface compression end at $x \simeq 2.43$, where a second local maximum of $\Gamma \simeq 0.91$ occurs.

For the two runs shown in this section, despite the decrease in aperture radius to $r_0 = 0.25$, both with and without solubility effects the surface surfactant concentration Γ remains well below the maximum surface concentration everywhere along the thread, whereas this was often attained in the simulations at the larger aperture openings of Secs. V B 1 and V B 2.

C. Comparison of simulation and experimental studies

In this section we compare results from our numerical simulations with results from the experiments reported by Moyle *et al.* [11].

1. Comparison of parameters

A complete list of apparatus dimensions and fluid properties for the experiments is given in Table I of Ref. [11], and those quantities that are needed for comparison are reproduced in Table I here. The values of dimensionless quantities such as the viscosity ratio λ and elasticity number E for the experimental data and as set in the simulations are given in Table II. Some quantities from the experimental and simulation data sets are in close agreement while others are not and require comment. For example, the baffle location of the simulations at $x = l = 2.0$ is within 1% of the analogous quantity in the experiments, which is $\Delta Z/a$ [see Fig. 2(a)]. Based on the apparatus dimensions in Table I the experimental value is 2.02, which is given together with the simulation value in Table II.

The dimensionless aperture radius r_0 is 0.20 in the experiments versus 0.50 in the simulations. We found tipstreaming in simulations when $r_0 = 0.25$, as described in Sec. V B 3, but at this and smaller values of the aperture radius it becomes increasingly difficult to determine if tipstreaming occurs at neighboring parameter values, and computational runs are costly due to the need for a small time

TABLE II. Values of dimensionless quantities in the experimental study by Moyle *et al.* [11] and in the simulations summarized in Fig. 16(b).

Dimensionless quantity	Value in experiments	Value in simulations
baffle location $x = l = \Delta Z/a$	2.02	2.0
aperture radius $r_0 = w_{or}/2a$	0.20	0.50
viscosity ratio $\lambda = \mu_1/\mu_2$	0.025	0.050
elasticity number $E = RT\Gamma_\infty/\sigma_0$	0.09	0.20
Péclet numbers $\mathrm{Pe}_s \simeq \mathrm{Pe} = Ua/D$	1.46×10^6	$\mathrm{Pe}_s = 10^3$
expansion parameter $\epsilon = \mathrm{Pe}^{-1/2}$	0.83×10^{-3}	
exchange coefficient[a] $J = DC_\infty/\Gamma_\infty U$	(4.30×10^{-7})–(4.30×10^{-5})	
scaled exchange coefficient[a] $J_0 = J/\epsilon$	(5.18×10^{-4})–(5.18×10^{-2})	(7.8×10^{-4})–10^{-1}
Biot number $\mathrm{Bi} = a\kappa_d/U$	4.16×10^{-10}	10^{-3}
partition coefficient[a] $K = \kappa_a C_\infty/\kappa_d$	(4.83×10^4)–(4.83×10^6)	(1.56×10^{-2})–2.0
modified Biot number[a] $\mathrm{Bi}K$	(2.0×10^{-5})–(2.0×10^{-3})	(1.56×10^{-5})–(2.0×10^{-3})

[a]Experimental values at CMC are estimated to be $K = 3.22 \times 10^5$, $J = 2.87 \times 10^{-6}$, $J_0 = 3.46 \times 10^{-3}$, and $\mathrm{Bi}K = 1.3 \times 10^{-4}$.

step. We have therefore kept the aperture radius fixed at the value $r_0 = 0.50$ of Sec. V B 2 and give an estimate of the influence of r_0 on the data below. The viscosity ratio λ is 0.025 in the experiments as opposed to 0.050 in the simulations. Simulations were made successfully at the smaller value $\lambda = 0.025$ but showed sufficiently little difference in the dynamics and data that λ was kept fixed at the value $\lambda = 0.050$ of the other simulations of this study.

The experimental data give an elasticity number $E = 0.09$ versus the value $E = 0.20$ used in the simulations. For tipstreaming to occur there must be a significant reduction in the local surface tension σ near the drop pole. However, in practice there is a maximum reduction that can be achieved with surfactants, and for an oil-water interface this is reported to be between about one-seventh [10] and one-tenth [6] of the clean surfactant-free value $\sigma = 1$. From the equation of state (5) this leads to a surface concentration Γ that satisfies

$$1 - \Gamma = e^{-(1-\sigma)/E}.$$

When E is small, at this minimum achievable surface tension Γ is exponentially close to both the theoretical maximum concentration, at which $\sigma = 0$, and the logarithmic singularity of the equation of state, at $\Gamma = 1$. Further, the sensitivity of surface tension to changes in surfactant concentration, given by

$$\frac{d\sigma}{d\Gamma} = \frac{-E}{1-\Gamma} = -Ee^{(1-\sigma)/E},$$

is exponentially large, and this can easily induce numerical instability in simulations of tipstreaming. We have set $E = 0.20$ to avoid this computational difficulty and note that this value is representative of many fluid-surfactant systems [6,31,41] and has been used in other numerical studies [16,17,20,40].

Surface and bulk Péclet numbers are believed to be nearly equal, and from the experimental data $\mathrm{Pe}_s \simeq Pe = 1.46 \times 10^6$, which leads to a value for the expansion parameter of the hybrid numerical method of $\epsilon = 0.83 \times 10^{-3}$. In the simulations, the surface Péclet number was set to 10^3. The numerical data and separate simulations with $\mathrm{Pe}_s = 0$ show that the influence of surface diffusion in the surfactant conservation equation (19) is negligible except in the region from the outer edge of the surfactant cap to the drop-thread merger, close to the end of the mother drop, where there is a substantial increase in Γ, e.g., at $1.64 \lesssim x \lesssim 1.90$ in Figs. 9(c) and 9(g), and the addition of some surface diffusion there is desirable to prevent overshoot in Γ.

The bulk-interface exchange coefficient J and equilibrium partition coefficient K are the only dimensionless parameters in the simulations that depend on the ambient bulk surfactant concentration C_∞, to which they are both directly proportional (see the definitions in Table II). The experimental data imply a range of J as shown in the table when C_∞ is varied. This leads to an estimate of the experimental range for the scaled exchange coefficient $J_0 = J/\epsilon$ that is very close to the range used in the surfactant exchange term of Eq. (19) in the simulations.

Chang and Franses [31] noted that in the context of an air-water interface the surface activity $K_L = \kappa_a/\kappa_d$ for common surfactants can vary widely, from 10^{-3} to 10^7 m^3/mol. From Table I, the value for the experimental data of $K_L = 3.22 \times 10^6$ is near the upper end of this range, and in predicting conditions for tipstreaming in their experiments Moyle *et al.* [11] justifiably neglected desorption of surfactant from the interface upstream of the base of a tipstreaming thread. However, in contrast, for the equilibrium initial conditions of the simulations the initial surface surfactant concentration $\Gamma_0 = K/(1+K)$, and for large K this is sufficiently close to $\Gamma = 1$, with a small surface tension everywhere on the interface, that the imposed flow cannot induce the surface tension gradients that are necessary to produce tipstreaming, and a mode of drop breakup that is similar to drop fracture occurs instead [6,15]. To induce tipstreaming in the simulations a range of smaller values of K must be chosen, and for the choice made here this gives an initial surface surfactant concentration Γ_0 in the range from 1.56×10^{-2} to 0.67.

Since the ratio J_0/K is independent of C_∞ it is held fixed throughout, and in the simulations $J_0/K = 5 \times 10^{-2}$. To compensate for the decrease in K relative to the experiments the Biot number Bi is increased in the simulations to $\mathrm{Bi} = 10^{-3}$ (see Table II). This choice closely reproduces the experimental values for the product BiK and the C_∞-independent ratio $J_0/\mathrm{Bi}K$, which is 25.8 in the experiments versus 50 in the simulations. In summary, the simulations closely replicate the experimental values of J_0 and BiK, but at larger values of Bi and smaller values of K, and so it is expected that the relative importance of adsorption is maintained while the role of desorption is enhanced. However, in the simulations desorption was seen in Sec. V B to be significant only on the downstream sections of an already developed tipstreaming thread, not in its initial formation by flow focusing.

2. Comparison of results

For the setup and geometry of the experiments a two-dimensional state space is introduced. This consists of a dimensionless bulk surfactant concentration $\bar{C}$ and a dimensionless flow rate or local capillary number $\bar{Q}$, which is based on the axial elongation flow rate near the focusing aperture, defined by

$$\bar{C} = \frac{\mu_0 a \kappa_a C_\infty}{RT\Gamma_\infty}, \quad \bar{Q} = \frac{20}{3}\frac{\mu_0 a^2 \phi Q_o}{(RT\Gamma_\infty)D_H^3 L}\left\{1 - \frac{w_{\mathrm{or}}}{2w_c}\right\}. \tag{30}$$

These are given at Eqs. (18) and (19) of Ref. [11], and quantities on the right-hand side are dimensional. In the expression of (30) for $\bar{Q}$, referring to the quantities indicated in Fig. 2, in which $Q_C \equiv Q_o$ and $Q_D \equiv Q_i$, we have the following: $\phi = Q_i/Q_o$ is the ratio of the dispersed phase volume flow rate Q_i to the exterior or continuous phase volume flow rate Q_o; D_H is the hydraulic diameter of the focusing aperture; and $L \equiv \Delta Z$, w_{or}, and $w_c \equiv W_{\mathrm{up}}$ are apparatus dimensions given in Table I. To compare the experimental and simulation results we use the closest analog for these quantities when an exact equivalent is not available: The dispersed phase channel half-width a in (30) is taken to be the radius of the initial undeformed spherical drop and is the length scale for nondimensionalization. The circular aperture of the simulations has hydraulic diameter $D_H = 2r_0$. The ratio of the aperture width w_{or} to the outer channel width w_c is such that $w_{\mathrm{or}}/2w_c \simeq 0.067$ in the experiments, which is neglected in approximating $\bar{Q}$ for the simulation data. The volume flow rate of the interior phase $Q_i = \phi Q_o$ is approximated by $Q_i = \pi r_{\mathrm{th}}^2 u_{\mathrm{th}}$, where r_{th} and u_{th} are, respectively, the radius and axial interfacial velocity of the tipstreaming thread at the center of the aperture. Since the ratio of the tipstreaming thread to aperture radii is small, this is independent of

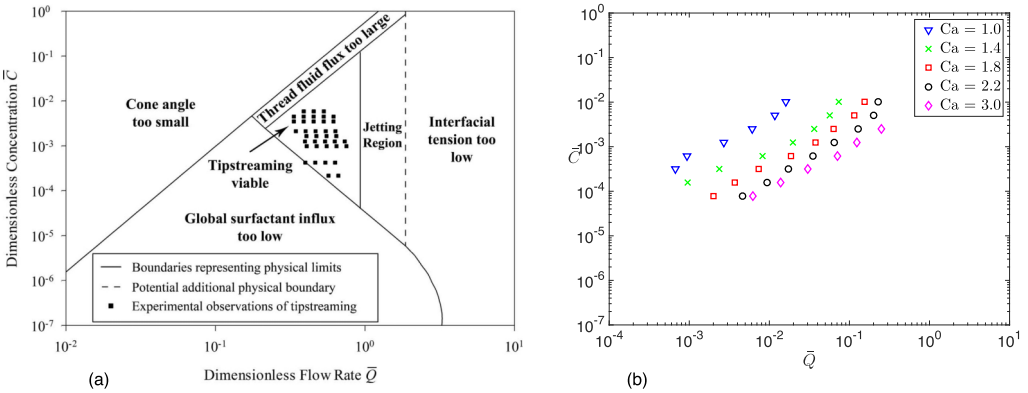

FIG. 16. Data in the $(\bar{Q}, \bar{C})$ state-space plane. (a) Conditions for tipstreaming observed experimentally by Moyle *et al.* [11] are denoted by squares. Lines denote boundaries outside which tipstreaming is not expected to occur based on a model of the setup and due to physical limits as indicated in the plot. [Panel (a) has been reproduced with permission from Ref. [11].] (b) Conditions for tipstreaming predicted by the flow-focusing simulations of this study, with symbol and capillary number Ca as indicated. Close agreement is found for the range of the dimensionless bulk surfactant concentration data $\bar{C}$. The difference in the range of values for the dimensionless flow rate $\bar{Q}$ is attributed mostly to the difference in the aperture radius r_0.

the precise form of the fluid velocity profile at the aperture, and in the simulation data $r_{\rm th}/r_o \lesssim 0.04$ in all computational runs. This leads to the analogous expression for the simulation data flow rate

$$\bar{Q} = \frac{5\pi}{6}\frac{\mu_0 a^2 r_{\rm th}^2 u_{\rm th}}{(RT\Gamma_\infty) r_0^3 L}. \tag{31}$$

So, in terms of the dimensionless velocity scale U and groups E, Bi, and K we have

$$\bar{C} = \frac{{\rm Bi}K}{E}, \quad \bar{Q} = \frac{5\pi}{6}\frac{r_{\rm th}^2 u_{\rm th}}{E r_0^3 l}, \tag{32}$$

where all quantities are now nondimensional.

Figure 16 shows points in the $(\bar{Q}, \bar{C})$ plane that correspond to tipstreaming conditions, as observed in the experiments in Fig. 16(a) and as predicted by the simulations in Fig. 16(b). About one week (wall clock time) was needed for each computational run, and from eight to ten runs were made for each of the imposed flow capillary number values Ca = 1, (0.4), 2.2, 3.0 as indicated in the inset. Some of these runs as well as runs at smaller Ca did not produce tipstreaming. The figure shows close agreement between the range of experimental and simulation data for the dimensionless bulk surfactant concentration $\bar{C}$ that produce tipstreaming. From the expression for $\bar{C}$ of Eq. (32) this is assisted by closely reproducing the experimental range of values for the product or modified Biot number BiK in the simulations, while the factor of 2 difference in E is partly covered up by the logarithmic scale of the figure.

By contrast, the range of $\bar{Q}$ for tipstreaming that is predicted by the simulations is not so close to the data of the experiments. An approximate range for the experimental data is $\bar{Q} \in (0.3, 1.0)$ compared with $\bar{Q} \in (0.001, 0.2)$ for the simulations. Based on the expression for $\bar{Q}$ of Eq. (32), if the volume flux of the tipstreaming thread, or equivalently $r_{\rm th}^2 u_{\rm th}$, is considered unaltered, the difference in aperture radius between the experiments ($r_0 = 0.2$) and the simulations ($r_0 = 0.5$) suggests a simple rescaling of the simulation data for $\bar{Q}$ by the factor 2.5^3, which puts it in the range $\bar{Q} \in (0.016, 3.13)$ and better reconciles the two data sets.

VI. CONCLUSION

We have investigated the influence of geometric flow focusing on the tipstreaming of a drop that is facilitated by soluble surfactant. A hybrid numerical method has been used to incorporate the effect of surfactant solubility. This resolves the fine spatial scale of a transition layer situated adjacent to the drop interface, in which the gradient of the dissolved surfactant concentration in the normal direction is large due to slow diffusion or large bulk Péclet number Pe. The method combines an asymptotic reduction in an interface-fitted coordinate system in the limit $\mathrm{Pe} \to \infty$ to resolve transport of dissolved surfactant in the layer with a method for solving two-phase flow with adsorbed interfacial surfactant. The two components are solved numerically, in parallel, and here the surface-based boundary integral method has been used to resolve the interfacial dynamics. To complement study of soluble surfactant in a microscale geometry the mixed-kinetic or finite Biot number form of the boundary condition for bulk-interface surfactant exchange has been used [31].

Here flow focusing is provided by transverse coaxial annular baffles that are placed symmetrically to either side of an isolated drop, flow is induced by a uniaxial extension at infinity, and the initially spherical drop has a surfactant-laden interface at equilibrium with its surroundings. Among the main findings are that a modest amount of focusing, for example, with dimensionless aperture radius $r_0 = 0.75$, at an imposed flow capillary number that is just sufficient to draw a surfactant-free drop through the aperture, the addition of a small amount of surfactant to the drop interface alters the mode of deformation at the drop tip to produce a narrow tipstreaming thread. The thread radius is significantly smaller than that produced at moderately higher initial surfactant concentrations without flow confinement and it decreases further with an increase of flow focusing down to the minimum aperture radius of the simulations reported, which is $r_0 = 0.25$. At this smallest aperture size, we find that a surfactant-free drop cannot be drawn through the aperture even at large capillary number, whereas at moderate capillary number a small initial surfactant concentration produces tipstreaming.

For the simulations of this study, when all other conditions including the aperture size are fixed, an increase in initial concentration of surfactant produces a thread that is longer at the time when the thread first pinches off when the surfactant is insoluble. With other conditions fixed, an increase of surfactant solubility due to an increase in Biot number produces a thread that is shorter at first pinch-off and this is attributed mainly to interface remobilization and desorption of surfactant from the thread, which leads to higher surface tension.

We have included results from two sets of simulations that are continued to times beyond first pinch-off of the thread by excising the small drops that break off from the thread's downstream end. These suggest that the process of thread breakup in the simulations is nearly periodic, at least for limited time intervals, and this is consistent with experimental observations [10,45].

The simulation results have been compared to experimental data on the conditions necessary for tipstreaming in the microscale flow device of Moyle *et al.* [11]. Differences between the dimensions and fluid properties of the simulations and experiment were noted in Sec. V C. Despite these, in a two-dimensional state space broad agreement for tipstreaming conditions has been found between the two data sets. Given additional apparent differences between the setup of the simulations and experiments, the agreement in the data is perhaps surprising. These differences include the following. (i) The simulations are for the evolution of an initially undeformed drop, in equilibrium, and with a given uniform surfactant concentration, so the context is that of an initial value problem. In contrast, in the experiments there is a continual supply of surfactant from one phase that is adsorbed onto an initially fresh surfactant-free interface at the merger of the dispersed and continuous phase feed channels [see Fig. 2(b)]. (ii) In the experimental data that is used for comparison, dissolved surfactant is supplied to the interface from the dispersed phase, while in the simulations it is soluble only in the continuous phase. Parallel channel sidewalls downstream of the aperture are also absent from the simulations but may not influence conditions for tipstreaming and the initial formation of a thread.

In the experiments, the point at which the cone of the interface merges with the base of the tipstreaming thread relative to the center of the aperture can be altered by adjusting the two phase volume flow rates. In a more recent experimental study this has been held nearly fixed via an active feedback control loop, thereby extending the time interval during which periodic behavior of thread breakup into nearly monodisperse droplets occurs [46]. In contrast, in the simulations, for given fluid properties, the location of the mother drop to thread merger is determined by the aperture radius r_0 and the imposed flow capillary number, and under the conditions of this study the point moves upstream relative to the aperture as r_0 is decreased.

We have shown the extent to which the large Pe hybrid method conserves surfactant in Sec. III B and we have included a note on the development of a surfactant plume downstream of a steady unconfined drop in Sec. IV.

ACKNOWLEDGMENTS

This work was supported in part by the NSF under Grants No. DMS-1412789 and No. DMS-1009105.

[1] G. I. Taylor, The formation of emulsions in definable fields of flow, Proc. R. Soc. London Ser. A **146**, 501 (1934).
[2] D. A. Edwards, H. Brenner, and D. T. Wasan, *Interfacial Transport Processes and Rheology* (Butterworth-Heinemann, Boston, 1991).
[3] K. Holmberg, Natural surfactants, Curr. Opin. Colloid Interface Sci. **6**, 148 (2001).
[4] E. Z. Ron and E. Rosenberg, Natural roles of biosurfactants, Environ. Microbiol. **3**, 229 (2001).
[5] H. A. Stone, Dynamics of drop deformation and breakup in viscous fluids, Annu. Rev. Fluid Mech. **26**, 65 (1994).
[6] R. A. de Bruijn, Tipstreaming of drops in simple shear flows, Chem. Eng. Sci. **48**, 277 (1993).
[7] J. J. M. Janssen, A. Boon, and W. G. M. Agterof, Influence of dynamic interfacial properties on droplet breakup in simple shear flow, AIChE J. **40**, 1929 (1994).
[8] J. J. M. Janssen, A. Boon, and W. G. M. Agterof, Influence of dynamic interfacial properties on droplet breakup in plane hyperbolic flow, AIChE J. **43**, 1436 (1997).
[9] S. L. Anna, Droplets and bubbles in microfluidic devices, Annu. Rev. Fluid Mech. **48**, 285 (2016).
[10] S. L. Anna and H. C. Mayer, Microscale tipstreaming in a microfluidic flow focusing device, Phys. Fluids **18**, 121512 (2006).
[11] T. M. Moyle, L. M. Walker, and S. L. Anna, Predicting conditions for microscale surfactant mediated tipstreaming, Phys. Fluids **24**, 082110 (2012).
[12] W.-C. Jeong, J.-M. Lim, J.-H. Choi, J.-H. Kim, Y.-J. Lee, S.-H. Kim, G. Lee, J.-D. Kim, G.-R. Yi, and S.-M. Yang, Controlled generation of submicron emulsion droplets via highly stable tip-streaming mode in microfluidic devices, Lab Chip **12**, 1446 (2012).
[13] M. R. Booty and M. Siegel, A hybrid numerical method for interfacial fluid flow with soluble surfactant, J. Comput. Phys. **229**, 3864 (2010).
[14] K. Xu, M. R. Booty, and M. Siegel, Analytical and computational methods for two-phase flow with soluble surfactant, SIAM J. Appl. Math. **73**, 523 (2013).
[15] Q. Wang, M. Siegel, and M. R. Booty, Numerical simulation of drop and bubble dynamics with soluble surfactant, Phys. Fluids **26**, 052102 (2014).
[16] C. D. Eggleton, T.-M. Tsai, and K. J. Stebe, Tip Streaming from a Drop in the Presence of Surfactants, Phys. Rev. Lett. **87**, 048302 (2001).
[17] I. B. Bazhlekov, P. D. Anderson, and H. E. H. Meijer, Numerical investigation of the effect of insoluble surfactants on drop deformation and breakup in simple shear flow, J. Colloid Interface Sci. **298**, 369 (2006).

[18] R. Suryo and O. A. Basaran, Tip streaming from a liquid drop forming from a tube in a co-flowing outer fluid, Phys. Fluids **18**, 082102 (2006).
[19] W. J. Milliken and L. G. Leal, The influence of surfactant on the deformation and breakup of a viscous drop: The effect of surfactant solubility, J. Colloid Interface Sci. **166**, 275 (1994).
[20] C. D. Eggleton and K. J. Stebe, An adsorption-desorption-controlled surfactant on a deforming droplet, J. Colloid Interface Sci. **208**, 68 (1998).
[21] Y. Wang, D. T. Papageorgiou, and C. Maldarelli, Increased mobility of a surfactant-retarded bubble at high bulk concentrations, J. Fluid Mech. **390**, 251 (1999).
[22] Y. Liao and J. B. McLaughlin, Bubble motion in aqueous surfactant solutions, J. Colloid Interface Sci. **224**, 297 (2000).
[23] S. N. Ghadiali, D. Halpern, and D. P. Gaver, A dual-reciprocity boundary element method for evaluating bulk convective transport of surfactant in free-surface flows, J. Comput. Phys. **171**, 534 (2001).
[24] F. Jin, N. R. Gupta, and K. J. Stebe, The detachment of a viscous drop in a viscous solution in the presence of a soluble surfactant, Phys. Fluids **18**, 022103 (2006).
[25] R. G. M. van der Sman and S. van der Graaf, Diffuse interface model of surfactant adsorption onto flat and droplet interfaces, Rheol. Acta **46**, 3 (2006).
[26] J. Zhang, D. M. Eckmann, and P. S. Ayyaswamy, A front tracking method for a deformable intravascular bubble in a tube with soluble surfactant transport, J. Comput. Phys. **214**, 366 (2006).
[27] M. Muradoglu and G. Tryggvason, A front-tracking method for computation of interfacial flows with soluble surfactants, J. Comput. Phys. **227**, 2238 (2008).
[28] K. E. Teigen, P. Song, J. Lowengrub, and A. Voigt, A diffuse-interface method for two-phase flows with soluble surfactants, J. Comput. Phys. **230**, 375 (2011).
[29] K.-Y. Chen and M.-C. Lai, A conservative scheme for solving coupled surface-bulk convection-diffusion equations with an application to interfacial flows with soluble surfactant, J. Comput. Phys. **257**, 1 (2014).
[30] S. Khatri and A.-K. Tornberg, An embedded boundary method for soluble surfactants with interface tracking for two-phase flows, J. Comput. Phys. **256**, 768 (2014).
[31] C.-H. Chang and E. I. Franses, Adsorption dynamics of surfactants at the air/water interface: A critical review of mathematical models, data, and mechanisms, Colloid Surf. A **100**, 1 (1995).
[32] H. Wong, D. Rumschitzki, and C. Maldarelli, On the surfactant mass balance at a deforming fluid interface, Phys. Fluids **8**, 3203 (1996).
[33] J. M. Rallison and A. Acrivos, A numerical study of the deformation and burst of a viscous drop in an extensional flow, J. Fluid Mech. **89**, 191 (1978).
[34] C. Pozrikidis, *Boundary Integral and Singularity Methods for Linearized Viscous Flow* (Cambridge University Press, Cambridge, 1992).
[35] G. K. Youngren and A. Acrivos, Stokes flow past a particle of arbitrary shape: A numerical method of solution, J. Fluid Mech. **69**, 377 (1975).
[36] B. K. Alpert, Hybrid Gauss-trapezoidal quadrature rules, SIAM J. Sci. Comput. **20**, 1551 (1999).
[37] H. A. Stone and L. G. Leal, Relaxation and breakup of an initially extended drop in an otherwise quiescent fluid, J. Fluid Mech. **198**, 399 (1989).
[38] H. A. Stone and L. G. Leal, The effects of surfactants on drop deformation and breakup, J. Fluid Mech. **220**, 161 (1990).
[39] R. G. Cox, The deformation of a drop in a general time-dependent fluid flow, J. Fluid Mech. **37**, 601 (1969).
[40] C. D. Eggleton, Y. P. Pawar, and K. J. Stebe, Insoluble surfactants on a drop in an extensional flow: A generalization of the stagnated surface limit to deforming interfaces, J. Fluid Mech. **385**, 79 (1999).
[41] J. Eastoe and J. S. Dalton, Dynamic surface tension and adsorption mechanisms of surfactants at the air/water interface, Adv. Colloid Interface Sci. **85**, 103 (2000).
[42] R. Pan, J. Green, and C. Maldarelli, Theory and experiment on the measurement of kinetic rate constants for surfactant exchange at an air/water interface, J. Colloid Interface Sci. **205**, 213 (1998).
[43] J. K. Ferri and K. J. Stebe, Which surfactants reduce surface tension faster? A scaling argument for diffusion-controlled adsorption, Adv. Colloid Interface Sci. **85**, 61 (2000).

[44] F. Jin, R. Balasubramaniam, and K. J. Stebe, Surfactant adsorption to spherical particles: The intrinsic length scale governing the shift from diffusion to kinetic-controlled mass transfer, J. Adhes. **80**, 773 (2004).

[45] W. Lee, L. M. Walker, and S. L. Anna, Role of geometry and fluid properties in droplet and thread formation processes in planar flow focusing, Phys. Fluids **21**, 032103 (2009).

[46] T. M. Moyle, L. M. Walker, and S. L. Anna, Controlling thread formation during tipstreaming through an active feedback control loop, Lab Chip **13**, 4534 (2013).